上海交通大学学位论文

磁星 X 射线偏振谱: 超强磁场环境下的辐射传输与真空量子效应研究

姓　名：郭图

学　号：**522072910011**

导　师：赖东

学　院：物理与天文学院

学科/专业名称：物理学 (强基计划)

申请学位层次：学士

2026 年 **06** 月

A Dissertation Submitted to

Shanghai Jiao Tong University for Bachelor Degree

POLARIZED X-RAY SPECTRA OF MAGNETARS: RADIATIVE TRANSFER AND VACUUM QUANTUM EFFECTS IN ULTRA-STRONG MAGNETIC FIELDS

Author: Tu Guo

Supervisor: Dong Lai

School of Physics and Astronomy

Shanghai Jiao Tong University

Shanghai, P. R. China

June, 2026

上海交通大学
学位论文原创性声明

本人郑重声明：所呈交的学位论文，是本人在导师的指导下，独立进行研究工作所取得的成果。除文中已经注明引用的内容外，本论文不包含任何其他个人或集体已经发表或撰写过的作品成果。对本文的研究做出重要贡献的个人和集体，均已在文中以明确方式标明。本人完全知晓本声明的法律后果由本人承担。

学位论文作者签名：郭图

日期：　2026 年 06 月 08 日

上海交通大学
学位论文使用授权书

本人同意学校保留并向国家有关部门或机构送交论文的复印件和电子版，允许论文被查阅和借阅。

本学位论文属于：

☑**公开论文**

☐ **内部论文**，保密 ☐1 年/☐2 年/☐3 年，过保密期后适用本授权书。

☐ **秘密论文**，保密 ___ 年（不超过 10 年），过保密期后适用本授权书。

☐ **机密论文**，保密 ___ 年（不超过 20 年），过保密期后适用本授权书。

（请在以上方框内选择打“✓”）

学位论文作者签名：郭图

指导教师签名：LaiDong

日期：　2026 年 06 月 08 日　　日期：　2026 年 06 月 08 日

摘　要

中子星是大质量恒星演化终点形成的一类致密残骸，具有极端的密度、磁场以及引力环境，而磁星是其中以超强磁场为主要特征的重要子类。在磁星中接近或超过量子电动力学临界磁场的强场环境中，真空极化、真空双折射等强场量子效应可能影响光子的产生、发射与传播行为。因此，探测磁星 X 射线偏振辐射既可约束磁星表面辐射与磁层结构等物理模型，也为在宏观尺度上检验强场量子电动力学效应提供了重要观测图景。

近年来，对若干静稳态磁星的观测揭示出了显著的软 X 射线偏振信号，其中部分发射源还表现出随光子能量变化显著的 90° 偏振角转动。本文建立了一个用于计算磁星能量依赖的软 X 射线偏振特征的半解析理论框架，并在该框架中统一纳入大气中的 QED 真空共振效应以及磁层中的共振康普顿散射（RCS）。本文从 RCS 的偏振辐射转移方程出发，以真空共振诱导的模式转换作为输入，在 RCS 光学深度的一阶近似下研究磁层等离子体密度（由磁层扭曲决定）、漂移速度、温度以及观测几何对观测辐射的影响。分析结果表明，磁层扭曲和等离子体漂移速度是控制 RCS 对偏振度的绝对值及其软 X 射线能段能量依赖影响的关键参数。本文发现，足够强的 RCS 可以抹平由真空共振造成的偏振角转动。此外，除 QED 真空共振效应外，由等离子体漂移速度（$\beta_0 \gtrsim 0.5$）导致的显著相对论效应也可能在谱中引入额外的 90° 偏振角转动。本文基于单次散射近似建立的计算框架避免了复杂的多维蒙特卡罗模拟，为磁星全表面辐射和转动相位分辨辐射建模提供了一种解析途径，并可为当前和未来的 X 射线偏振观测任务提供理论支持。

关键词：中子星，磁星，X 射线偏振，辐射传输，量子电动力学，真空双折射，共振康普顿散射

ABSTRACT

Neutron stars are compact remnants formed at the endpoints of massive stellar evolution and are characterized by extreme density, magnetic-field strength, and gravitational environments. Magnetars constitute an important subclass distinguished by ultra-strong magnetic fields. In the strong magnetic fields of magnetars, which are near or above the quantum electrodynamics (QED) critical field, vacuum polarization and vacuum birefringence can affect photon generation, emission, and propagation. X-ray polarimetry of magnetars can therefore constrain models of surface emission and magnetospheric structure, while also providing a promising route for testing strong-field QED on macroscopic scales.

Recent observations have revealed significant soft X-ray polarization from several quiescent magnetars, including the intriguing 90° polarization angle (PA) swing as a function of photon energy for some sources. We present a general semi-analytical framework for calculating energy-dependent soft X-ray polarization signatures from magnetars, consistently incorporating both QED vacuum resonance in the atmosphere and resonant Compton scattering (RCS) in the magnetosphere. Starting from the polarized radiative transfer equation for RCS and treating vacuum-resonance-induced mode conversion as an input, we employ a first-order approximation in RCS optical depth to evaluate the effects of magnetospheric plasma density (which depends on magnetic twist), drift velocity, temperature, and viewing geometry on the observed radiation. Our analysis reveals that magnetic twist and plasma drift velocity are the critical parameters controlling the impact of RCS on both the absolute polarization degree and its variation across the soft X-ray spectrum. We find that sufficiently strong RCS can wash out the PA swing caused by vacuum resonance. Furthermore, in addition to the QED vacuum resonance effect, significant relativistic signatures arising from plasma drift velocity ($\beta_0 \gtrsim 0.5$) may introduce an extra 90° PA swing in the spectrum. Our calculation framework, based on the single-scattering approximation, bypasses the need for complex, multidimensional Monte Carlo simulations, providing an analytical pathway for modeling full-surface emission and rotational-phase-resolved radiation from magnetic neutron stars in support of current and future X-ray polarization missions.

Key words: Neutron stars, Magnetars, X-ray polarization, Radiative transfer, Quantum electrodynamics, Vacuum birefringence, Resonant Compton scattering

CONTENTS

1 Introduction

1.1 Foreword

Neutron stars are compact remnants formed in the final evolutionary stages of massive stars [1]. For stars with sufficiently large initial masses, usually $M \gtrsim 8M_{\odot}$, nuclear burning can proceed through hydrogen and helium burning to the synthesis of heavier elements near the iron peak. Since iron-peak nuclei have among the largest binding energies per nucleon, further fusion can no longer provide sufficient energy support. Once the core loses pressure support, it undergoes gravitational collapse; the subsequent bounce, shock propagation, and neutrino heating may lead to a core-collapse supernova. If the collapsed core remains below the maximum mass of a stable neutron star, the remnant can become a neutron star rather than a black hole. Neutron stars therefore connect stellar evolution, supernova explosions, dense-matter physics, and gravitational-wave astrophysics.

A typical neutron star has mass $M \sim 1$–$2M_{\odot}$ and radius $R \sim 10$–15 km, implying mean densities comparable to or above nuclear density and a compactness for which general-relativistic effects are essential. Neutron stars also possess rapid rotation and strong magnetic fields. Their fast spin mainly follows from angular-momentum conservation during collapse [2, 3], while their magnetic fields may originate from magnetic-flux conservation and turbulent dynamo amplification during formation [4, 5]. Surface magnetic fields range from 10^{11}–10^{13} G in ordinary radio pulsars to 10^{14}–10^{15} G in magnetars, with possibly stronger local fields. As a result, atmospheric emission, magnetospheric plasma motion, radiative processes, and polarization propagation are all strongly shaped by the magnetic-field geometry.

Based on their observational manifestations, neutron stars are divided into several related populations. The spin period and its time derivative provide an estimate of the dipole surface magnetic field through the spin-down rate, helping distinguish different classes. Radio pulsars are mainly powered by rotational-energy loss and observed through periodic nonthermal radio emission; accreting neutron stars in binaries radiate primarily through the gravitational energy released by accretion; central compact objects, isolated thermally emitting neutron stars, millisecond pulsars, and rotation-powered X-ray pulsars reflect different ages, field strengths, and evolutionary channels. Magnetars are dis-

tinguished by persistent high-energy emission, bursts, and long-term activity that cannot usually be powered by spin-down alone, but are instead attributed to the energy reservoir and evolution of ultra-strong magnetic fields.

Magnetars are isolated neutron stars endowed with extremely strong magnetic fields [6–9]. Their surface dipole magnetic fields inferred from spin-down measurements typically reach $B_{\rm dip} \sim 10^{14}$–10^{15} G. Historically, the magnetar subclasses of Soft Gamma Repeaters (SGRs) and Anomalous X-ray Pulsars (AXPs) were distinguished by their burst behaviors, but both emit persistent soft X-rays (0.5–10 keV) in quiescence with typical luminosities of $L_{\rm X} \sim 10^{33}$–10^{36} erg s^{-1}, much larger than their spin-down luminosities. Their quiescent X-ray spectra are commonly described by a combination of a thermal blackbody with $kT \sim 0.5$–1 keV and a non-thermal power law with photon index $\Gamma \sim 2$–4 [10]. They also emit hard X-rays extending to ~ 100 keV, indicating an active corona surrounding magnetars [9]. Despite the rich phenomenology, the integrated X-ray spectrum alone is often inadequate to disentangle the degeneracy among different emission mechanisms and magnetospheric physics. However, X-ray polarization measurements can help break this degeneracy and provide constraints on various physical parameters and magnetospheric structure [11–13].

The observed phenomenology of magnetars can generally be understood as the outcome of the coupling among the internal ultra-strong magnetic field, the dense condensed crust, and the external magnetosphere. Strong magnetic fields can store enormous electromagnetic energy inside neutron stars. As the magnetic field evolves slowly, stresses may accumulate in the crust and lead to fractures or plastic deformation, i.e., starquakes, thereby triggering short X-ray/soft gamma-ray bursts. Crustal displacement can also twist magnetic field lines anchored on the surface and form a twisted magnetosphere with a toroidal field component [see 14]. Meanwhile, charged particles flowing along magnetic field lines in the twisted magnetosphere can interact with photons emitted from the surface, modifying both the spectrum and polarization state of the surface radiation and consequently affecting the final observed signal. Magnetar radiation is therefore not simply blackbody emission from the surface, but rather the combined result of atmospheric emission, magnetospheric scattering, propagation geometry, and general-relativistic propagation.

The ultra-strong magnetic-field environment of magnetars also makes them natural laboratories for testing strong-field quantum electrodynamics (QED) effects on macroscopic scales. In classical electrodynamics, vacuum does not modify the propagation properties of electromagnetic waves. In QED, however, high-energy photons can fluctuate into virtual electron–positron pairs, and in the presence of a strong background magnetic field the interaction between the electromagnetic field and these virtual pairs polarizes the vacuum [15]. This vacuum polarization thus modifies photon propagation. As a result, the vacuum in a strong magnetic field behaves as an effective birefringent medium, a phenomenon known as vacuum birefringence. When the background magnetic field approaches or exceeds the quantum critical field $B_Q = m_e^2 c^3/(e\hbar) \simeq 4.4 \times 10^{13}$ G, vacuum polarization can significantly alter the polarization eigenmodes and propagation phases of photons. For terrestrial strong-field laser experiments, it is extremely difficult to achieve both such field strengths and observable propagation lengths [16, 17]. Magnetar surfaces, by contrast, naturally possess large-scale magnetic fields with $B \gtrsim B_Q$, thereby providing a unique opportunity to test strong-field QED on macroscopic scales [18, 19].

In recent years, the Imaging X-ray Polarimetry Explorer (IXPE) mission [20] from NASA has enabled polarimetry measurements in the 2–8 keV band, delivering high-significance detections across multiple sources, including several magnetars. The IXPE observations of magnetars have revealed two representative types of energy-dependent polarization behavior in the soft X-ray band: one class [e.g., 4U 0142+61 in 21] exhibits a sharp $\sim 90^\circ$ polarization angle (PA) swing at around 5 keV, while the other [e.g., 1RXS J170849.0-400910 in 22] maintains a nearly energy-independent constant polarization angle.

The importance of X-ray polarimetric observations of magnetars lies in the fact that polarization encodes not only the mode information at emission, but also the mode evolution experienced by photons as they propagate through a magnetized plasma modified by quantum vacuum effects. Conventional spectral observations mainly measure the distribution of total photon counts as a function of energy, while timing observations primarily measure flux variations with rotational phase or burst evolution. Polarimetric observations provide two additional dimensions, the polarization degree and polarization angle, and therefore offer a more direct way to distinguish different emission and propagation

mechanisms and to test whether the polarization angle exhibits energy-dependent variations induced by QED vacuum resonance or magnetospheric propagation effects. Magnetar spectropolarimetry is thus both an important diagnostic of neutron-star radiation models and a potential observational probe of strong-field QED on macroscopic scales.

1.2 The main content of this paper

To explain these spectral polarization features from IXPE results, current theoretical efforts mainly focus on two physical mechanisms: emission from a condensed surface [13, 21], followed by resonant Compton scattering (RCS) in the magnetosphere [11, 23], and the mode conversion effect via vacuum resonance in the atmospheric plasma under strong magnetic fields [24–27]. A condensed surface requires sufficiently low temperature and high surface binding energy, which remain uncertain [28–31]. RCS by charged particles in a twisted magnetosphere can modify the emergent radiation spectrum and polarization profile. This process has been modeled in both semi-analytical 1D frameworks [32] and multidimensional Monte Carlo simulations with detailed spectral fits [33–36], and further extended to polarization predictions [11, 13, 23, 37].

Vacuum resonance, on the other hand, arises from the competition between plasma-induced birefringence and vacuum birefringence due to quantum electrodynamics (QED) in strong magnetic fields. When a photon crosses the resonant layer, it may undergo adiabatic mode conversion, leading to a significant change in the polarization [24, 25, 38]. After leaving the atmosphere, the photon may experience significant RCS in the extended magnetosphere or corona, leading to further modifications in polarization.

In the context of macroscopic tests of strong-field QED, vacuum resonance is of particular importance. Although the quantum correction to the dielectric tensor in the strong magnetic fields of magnetars is small by itself, the eigenmode evolution of propagating photons can be strongly affected when this correction cancels the plasma contribution and produces a resonance [25, 38]. Vacuum resonance does not simply modify the radiation intensity; instead, it can change the identity of the polarization eigenmodes near a specific energy, appearing observationally as a sudden energy-dependent rotation of the polarization angle or a significant change in the polarization degree [for observational evidence, see 21]. Meanwhile, the adiabatic evolution of photon eigenmodes with respect to the

local magnetic-field direction tends to align polarization vectors from different regions of the magnetosphere, rather than allowing them to cancel through random orientations, and can therefore produce a significant nonzero net polarization [e.g., 39]. If such energy-dependent polarization features can be connected to magnetar atmospheric parameters, magnetic-field strength, and viewing geometry, they may provide astrophysical evidence for vacuum birefringence and vacuum polarization on macroscopic scales. However, magnetospheric RCS may also weaken, obscure, or reshape this QED signal, and the two effects must therefore be treated together rather than studying vacuum resonance in the surface atmosphere alone.

The theoretical description of photon production, propagation, and scattering requires the language of radiative transfer. Radiative transfer describes how radiation intensity evolves in space, direction, and frequency under the combined effects of absorption, emission, scattering, and propagation geometry. In ordinary stellar atmospheres, radiative transfer already requires one to treat the temperature structure, opacity, and angular distribution. In neutron-star and magnetar environments, strong magnetic fields make the medium anisotropic, and the two polarization eigenmodes of photons have different opacities and scattering cross sections, further increasing the complexity of the problem. Polarized radiative transfer must therefore track the mode-resolved intensity, polarization degree, polarization angle, and conversions between different modes simultaneously.

Radiative transfer in magnetars also has an intrinsically multiscale character. Photons are first generated in a high-density, strong-field atmosphere or near a condensed surface. They then pass through the vacuum-resonance region and may undergo adiabatic or nonadiabatic conversion between the X and O modes [25, 26]. After leaving the surface, photons may further experience resonant Compton scattering with electrons moving along magnetic field lines in the magnetosphere. Each of these processes can modify the spectrum and polarization, while the final observed signal is also affected by the hot-spot location, viewing angle, rotational phase, light bending, and magnetospheric geometry. A self-consistent and controlled model of magnetar polarization must therefore incorporate surface emission, QED vacuum resonance, general-relativistic propagation, and magnetospheric scattering within a single computational framework.

In this work, we present a general three-dimensional semi-analytical framework that

unifies the treatment of vacuum resonance in the atmosphere and RCS in the magnetosphere, with the goal of obtaining the soft X-ray polarization of magnetic neutron stars. To preserve the physical transparency and geometric modularity of our calculation without relying on full Monte Carlo simulations of radiative transport, we use the single-scattering approximation. To focus on the key physics, we adopt simplified yet testable idealized assumptions for the polarized surface emission, including the vacuum resonance effect. The structure of this paper is as follows: Section 2 introduces the physical model and computational procedure; Section 3 presents the validation of our fiducial model; Section 4 investigates the X-ray polarization signals for various physical parameters; Section 5 provides the summary and outlook.

1.3 The significance of this work

The goal of this work is to construct a concise, self-consistent, and controlled semi-analytical model for studying the polarization signatures of soft X-ray radiation from magnetar surfaces, as well as the effects of QED vacuum resonance and magnetospheric resonant Compton scattering on these signatures. The model is based on the single-scattering approximation to the radiative transfer equation, avoiding complex multidimensional Monte Carlo simulations while preserving physical transparency and controllability of individual effects. Within the parameter regime where the single-scattering approximation is valid, this framework provides an analytical pathway for modeling the spectra and polarization of X-ray radiation from magnetar surfaces, offers an intuitive theoretical picture for interpreting the magnetar X-ray spectropolarimetric behavior accumulated by IXPE, and can support current and future X-ray polarimetric missions targeting magnetars. The transparency and controllability of the model also allow us to separate different physical mechanisms and their effects on the observed signal, thereby providing a theoretical tool for studies of magnetar radiation mechanisms, magnetospheric structure, and strong-field QED effects.

1.4 Summary

This section has started from the background of stellar evolution, neutron-star formation, and neutron-star classification, and has introduced the basic physical properties

and observational phenomenology of magnetars. We have also clarified the importance of X-ray polarimetric observations of magnetars, whose significance lies not only in testing magnetar radiation models but also in probing QED effects on macroscopic scales. We then reviewed the two main physical mechanisms currently used to interpret IXPE observations, namely resonant Compton scattering in the magnetosphere and QED vacuum resonance in the atmosphere, as well as their effects on X-ray polarization. Finally, this section has outlined the main content and significance of this work: to build a concise and controlled semi-analytical physical model that unifies QED vacuum resonance in the atmosphere and resonant Compton scattering in the magnetosphere within a single computational framework, in order to study their effects on the X-ray spectropolarimetric signatures of magnetars.

2 Physical Framework

To model how resonant Compton scattering and QED vacuum resonance jointly shape the X-ray polarization from magnetars, we distinguish the main physical processes with their characteristic locations. This section presents our physical framework for the global magnetosphere, polarized emission and propagation, RCS formalism, and computational workflow.

2.1 Global magnetosphere model

One of the key characteristics of magnetars is the presence of a highly twisted and dynamically evolving toroidal magnetic field in a magnetar's magnetosphere [14]. This arises from the magnetic stress built up in the crust, which induces instabilities, leading to displacement of surface elements and distortion of the magnetic field lines anchored on them. Thompson et al. [14] present a general self-similar, force-free, globally twisted magnetic field model that has been widely used in previous studies [e.g., 11, 33, 34]. In this model, solving the force-free condition $(\nabla \times \mathbf{B}) \times \mathbf{B} = 0$ outside an axisymmetric sphere yields a sequence of globally twisted self-similar magnetic-field solutions that forms a one-parameter family. In spherical coordinates (r, θ, ϕ), the magnetic-field solution can be written as

$$\mathbf{B}(r,\theta) = \frac{B_{\rm p}}{2}\left(\frac{R}{r}\right)^{2+p}\mathbf{F}(\cos\theta), \tag{2-1}$$

where $B_{\rm p}$ is the surface polar dipole field strength, R is the magnetar radius, and p is a non-dimensional parameter that controls the twisting of the magnetic field. The spherical components of the vector $\mathbf{F}$ can be expressed in terms of the function $f(\cos\theta)$:

$$\mathbf{F} = \left(-f'(\cos\theta), \frac{p f(\cos\theta)}{\sin\theta}, \sqrt{\frac{pC(p)}{p+1}}\frac{f^{1+1/p}}{\sin\theta}\right), \tag{2-2}$$

where $C(p)$ is a constant that depends only on p. The function $f(\cos\theta)$ satisfies the following Grad-Shafranov equation:

$$\sin^2\theta f'' + C f^{1+2/p} + p(p+1) f = 0, \tag{2-3}$$

with the boundary conditions $f'(0)=0$, $f'(1)=-2$, and $f(1)=0$. In addition, the degree of magnetospheric twist can also be characterized by the global twist angle $\Delta\phi$, defined as the azimuthal angle swept by a magnetic field line from the magnetic north pole to the south pole:

$$\Delta\phi = 2\lim_{\theta_0\to 0}\int_{\theta_0}^{\pi/2}\frac{B_\phi}{B_\theta}\frac{\mathrm{d}\theta}{\sin\theta}. \tag{2-4}$$

For the purposes of this work, we adopt a simple parametrized model in which a toroidal component proportional to the poloidal field is added, i.e.,

$$\mathbf{B}(\mathbf{r}) = \frac{B_\mathrm{p}}{2}\left(\frac{r}{R}\right)^{-3}(2\cos\theta, \sin\theta, \xi_\tau\sin\theta), \tag{2-5}$$

where the parameter ξ_τ quantifies the global twist (hence the current distribution). This choice is not strictly force-free, but it captures a quasi-static configuration adequate for our semi-analytic treatment.

We assume that the magnetospheric plasma consists of a single charge species and that the ions are stationary. It should also be noted that kinetic modeling of external currents in magnetars [40–43] suggests that the real magnetospheric plasma may be a denser electron–positron pair plasma (see Section 5 for further discussion). Given $\mathbf{B}$, from Maxwell's equation $\nabla\times\mathbf{B} = 4\pi/c\,\mathbf{j} = 4\pi/c\,(-n_e e\mathbf{v}_e)$, the spatial distribution of current-carrying electrons along the closed field lines in the NS frame is prescribed as [14, 34, 37]

$$n_e(\mathbf{r},\beta_0) = \frac{(\xi_\tau\beta_0^{-1})\,B(\mathbf{r})}{4\pi e\,r}, \tag{2-6}$$

where $B=|\mathbf{B}(\mathbf{r})|$. We denote by $\beta_e\in(-1,1)$ the electron velocity (normalized by c) along the field lines, and $\beta_0=|\langle\beta_e\rangle|$ is the mean drift speed.

To determine the full phase-space distribution, we assume a one-dimensional, relativistic, thermal (Maxwell–Jüttner) velocity distribution along the field line, boosted by β_0 [see also 34, 44]. Starting from the standard Maxwell–Jüttner distribution in the rest frame, the normalized 1D velocity distribution function can be expressed as

$$f_0(\beta_e)\,\mathrm{d}\beta_e = \frac{\gamma_e^3\exp(-\gamma_e/\Theta_e)}{2K_1(1/\Theta_e)}\mathrm{d}\beta_e, \tag{2-7}$$

where $\Theta_e = kT_e/m_ec^2$ and K_1 is the modified Bessel function, which can be calculated as

$$K_1(z) = z\int_1^\infty \mathrm{e}^{-zt}(t^2-1)^{1/2}\mathrm{d}t. \tag{2-8}$$

Eq. (2-7) describes the electron velocity distribution in the reference frame moving along the magnetic field lines with mean drift speed β_0. When transforming this distribution function to the neutron-star frame, the velocity transformation satisfies $\beta_e^{(\mathrm{rest})} = (\beta_e-\beta_0)/(1-\beta_e\beta_0)$. Using the Lorentz invariance of the probability element, the velocity distribution function in the neutron-star frame, $f_1(\beta_e) \equiv f_0(\beta_e^{\mathrm{rest}})\,\mathrm{d}\beta_e^{\mathrm{rest}}/\mathrm{d}\beta_e$, is obtained as

$$f_1(\beta_e)\,\mathrm{d}\beta_e = \frac{\gamma_0\gamma_e^3(1-\beta_e\beta_0)\exp(-\gamma'/\Theta_e)}{2K_1(1/\Theta_e)}\,\mathrm{d}\beta_e, \tag{2-9}$$

with $\gamma' = \gamma_e\gamma_0(1-\beta_e\beta_0)$. This boosting captures the net drift from the magnetic north to south. We assume that the magnetospheric temperature T_e is uniform, and treat T_e and β_0 as free parameters. Overall, our magnetosphere model is characterized by three parameters: (ξ_τ, β_0, T_e).

2.2 Seed polarized radiation and propagation

2.2.1 QED vacuum birefringence

Quantum electrodynamics shows that in environments above the quantum critical field $B_\mathrm{Q} = 4.4\times10^{13}$ G near magnetar surfaces, vacuum polarization can have a non-negligible influence on the dielectric properties of the vacuum [e.g., 15, 45, 46]. From the perspective of quantum field theory, when the one-loop QED correction is added to the electromagnetic-field Lagrangian, the effective electromagnetic Lagrangian can be written as $\mathcal{L} = \mathcal{L}_0 + \mathcal{L}_1$ [46]. In terms of the Lorentz invariants of the electromagnetic field

$$I = F_{\mu\nu}F^{\mu\nu} = 2\left(|\mathbf{B}|^2 - |\mathbf{E}|^2\right) \tag{2-10}$$

and

$$K = \left(\frac{1}{2}\varepsilon^{\lambda\rho\mu\nu}F_{\lambda\rho}F_{\mu\nu}\right)^2 = -(4\mathbf{E}\cdot\mathbf{B})^2, \tag{2-11}$$

the unperturbed electromagnetic Lagrangian and the one-loop QED correction in the weak-field limit are given by [47]

$$\begin{aligned}\mathcal{L}_0 &= -\frac{1}{4}I,\\ \mathcal{L}_1 &= E_{\mathrm{Q}}^2\frac{e^2}{hc}\left[\frac{1}{E_{\mathrm{Q}}^4}\left(\frac{1}{180}I^2-\frac{7}{720}K\right)+\frac{1}{E_{\mathrm{Q}}^6}\left(\frac{13}{5040}KI-\frac{1}{630}I^3\right)\cdots\right],\end{aligned} \tag{2-12}$$

where $B_{\mathrm{Q}} = E_{\mathrm{Q}} = m_e^2c^3/e\hbar \approx 4.4\times10^{13}$ G. Defining the dimensionless parameter $\xi \equiv E_{\mathrm{Q}}^{-1}\sqrt{I/2}$ to characterize the field strength, and adopting the small-K expansion of the Lagrangian correction derived by Heyl et al. [48],

$$\mathcal{L}_1 = \mathcal{L}_1(I,0) + K\left.\frac{\partial\mathcal{L}_1}{\partial K}\right|_{K=0} + \frac{K^2}{2}\left.\frac{\partial^2\mathcal{L}_1}{\partial K^2}\right|_{K=0} + \cdots, \tag{2-13}$$

the first two terms of this expansion are

$$\begin{aligned}\mathcal{L}_1(I,0) &= \frac{e^2}{hc}\frac{I}{2}X_0\left(\frac{1}{\xi}\right),\\ \left.\frac{\partial\mathcal{L}_1}{\partial K}\right|_{K=0} &= \frac{e^2}{hc}\frac{1}{16I}X_1\left(\frac{1}{\xi}\right),\end{aligned} \tag{2-14}$$

where the dimensionless functions X_0 and X_1 are defined as follows [46]:

$$\begin{aligned}X_0(x) =& 4\int_0^{x/2-1}\ln(\Gamma(v+1))\mathrm{d}v+\frac{1}{3}\ln\left(\frac{1}{x}\right)+2\ln4\pi-\left(4\ln A+\frac{5}{3}\ln2\right)\\ &-\left[\ln4\pi+1+\ln\left(\frac{1}{x}\right)\right]x+\left[\frac{3}{4}+\frac{1}{2}\ln\left(\frac{2}{x}\right)\right]x^2,\\ X_1(x) =& -2X_0(x)+xX_0^{(1)}(x)+\frac{2}{3}X_0^{(2)}(x)-\frac{2}{9}\frac{1}{x^2},\end{aligned} \tag{2-15}$$

with $\ln A \approx -0.2488$.

When the vacuum is treated as a polarizable medium, the macroscopic effective fields can be written, according to Heaviside-Lorentz electromagnetic medium theory, as

$$\mathbf{D} = \frac{\partial\mathcal{L}}{\partial\mathbf{E}} = \mathbf{E}+\mathbf{P},\quad \mathbf{H} = -\frac{\partial\mathcal{L}}{\partial\mathbf{B}} = \mathbf{B}-\mathbf{M},\quad \mathbf{P} = \frac{\partial\mathcal{L}_1}{\partial\mathbf{E}},\quad \mathbf{M} = \frac{\partial\mathcal{L}_1}{\partial\mathbf{B}}. \tag{2-16}$$

Given dielectric tensor ε and the inverse permeability tensor μ', which are respectively

defined by

$$D_i = \varepsilon_{ij} E_j, \quad H_i = \mu'_{ij} B_j, \tag{2-17}$$

solving the above macroscopic field equations and substituting the definitions of I and K gives

$$\begin{aligned} \varepsilon_{ij} =& \delta_{ij} - 4\frac{\partial \mathcal{L}_1}{\partial I}\delta_{ij} - 32\frac{\partial \mathcal{L}_1}{\partial K} B_i B_j, \\ \mu'_{ij} =& \delta_{ij} - 4\frac{\partial \mathcal{L}_1}{\partial I}\delta_{ij} + 32\frac{\partial \mathcal{L}_1}{\partial K} E_i E_j. \end{aligned} \tag{2-18}$$

Substituting the expansion of $\mathcal{L}_1$ under the weak-field approximation yields the approximate expressions for ε and μ', a result also given by Klein et al. [49]:

$$\begin{aligned} \varepsilon_{ij} =& \delta_{ij} + \frac{1}{45\pi}\frac{\alpha}{B_k^2}\left[2(E^2 - B^2)\delta_{ij} + 7B_i B_j\right], \\ \mu'_{ij} =& \delta_{ij} + \frac{1}{45\pi}\frac{\alpha}{B_k^2}\left[2(E^2 - B^2)\delta_{ij} - 7E_i E_j\right], \end{aligned} \tag{2-19}$$

where $\alpha = e^2/\hbar c \approx 1/137$ is the fine-structure constant. Near magnetar surfaces, the electric field is usually much smaller than the magnetic field, so the contribution from the E^2 terms can be neglected, yielding the following simplified expressions [11]:

$$\begin{aligned} \varepsilon &= \mathbb{I} + \varepsilon^{(v)} = (1+a)\mathbb{I} + q\widehat{\mathbf{B}}\widehat{\mathbf{B}}, \\ \mu' &= \mathbb{I} + \mu'^{(v)} = (1+a)\mathbb{I} + m\widehat{\mathbf{B}}\widehat{\mathbf{B}}. \end{aligned} \tag{2-20}$$

The coefficients q, m, a are approximately $a = -2\delta, q = 7\delta, m = -4\delta$, where δ is given by

$$\delta = \frac{\alpha}{45\pi}\left(\frac{B}{B_{\rm Q}}\right)^2 \approx 3\times 10^{-4}\left(\frac{B}{10^{14}\ {\rm G}}\right)^2. \tag{2-21}$$

Thus, the weak-field approximation remains valid throughout the regions relevant to magnetar radiation generation and propagation.

2.2.2 Surface emission model from vacuum resonance

The bulk of the 2–8 keV photons probed by IXPE originate from the magnetar surface. To model the spectrum and polarization of the surface emission, it is necessary to construct self-consistent magnetic NS atmosphere models that take QED effects into account [e.g., 18, 25, 37, 50–52]. Here we summarize the key features of this emission [see

also 26].

X-ray photons (with $E = \hbar\omega \ll E_B = \hbar\omega_B = \hbar eB/m_e c = 1158 B_{14}$ keV) propagating in the magnetized NS atmospheric plasma have two polarization modes: the ordinary mode (O-mode) is mostly polarized parallel to the $\mathbf{k}-\mathbf{B}$ plane, while the extraordinary mode (X-mode) is perpendicular to it, where $\mathbf{k}$ is the photon wave vector and $\mathbf{B}$ is the external magnetic field. The two modes have very different absorption and scattering opacities, with $\kappa_{\rm X-mode} \sim u_e^{-1}\kappa_{\rm O-mode}$, where $u_e \equiv (\omega_B/\omega)^2 \gg 1$. Thus, the two modes have very different photosphere densities, with $\rho_{\rm X-mode} \gg \rho_{\rm O-mode}$, and the emergent radiation from the NS surface is dominated by the X-mode.

However, the effect of vacuum polarization can change the above picture significantly. In particular, the "competition" between QED-induced vacuum birefringence and plasma-induced birefringence gives rise to a vacuum resonance; for a photon of energy E, this occurs at the density

$$\rho_V \simeq 0.964\, Y_e^{-1} B_{14}^2 E_1^2 f^{-2}\ {\rm g\ cm^{-3}}, \tag{2-22}$$

where $Y_e = \langle Z/A\rangle$ is the electron fraction, $E_1 = E/(1\ {\rm keV})$, and $f = f(B)$ is a slowly varying function of B and is of order unity.

For $\rho \gtrsim \rho_V$ (where the plasma effect dominates the dielectric tensor) and $\rho \lesssim \rho_V$ (where vacuum polarization dominates), the photon modes (for typical $\theta_{\rm kB} \neq 0$) are almost linearly polarized, i.e., the linear X-mode and O-mode; at $\rho = \rho_V$, however, the normal modes become circularly polarized. The importance of this vacuum resonance lies in the mode-conversion phenomenon [24, 25]: an X-mode photon emerging from its photosphere (at $\rho_{\rm X-mode}$) and propagating outward can convert to the O-mode at ρ_V, provided that its energy satisfies

$$E \gtrsim E_{\rm ad} = 2.52\left(f\tan\theta_{kB}\right)^{2/3}\left(\frac{1\ {\rm cm}}{H_\rho}\right)^{1/3}{\rm keV}, \tag{2-23}$$

where $H_\rho = |{\rm d}s/{\rm d}\ln\rho|$ is the density scale height (evaluated at $\rho = \rho_V$) along the ray.

According to the derivation in [25], the mode conversion probability can be calculated as

$$P_{\rm conv} = 1 - P_{\rm J} = 1 - \exp\left[-\frac{\pi}{2}\left(\frac{E}{E_{\rm ad}}\right)^3\right]. \tag{2-24}$$

A low-energy ($E \lesssim E_{\rm ad}$) photon would not experience this conversion.

In typical magnetar atmospheres, $\rho_{\rm X-mode} \gg \rho_V$ is always satisfied. Depending on the relative locations of the O-mode photosphere and vacuum resonance, the X-ray polarization signatures are qualitatively different. Assuming a fully ionized atmosphere (with ion charge Ze and mass Am_p), Lai [26] finds the ratio

$$\rho_V/\rho_{\rm O-mode} = (B/B_{\rm ov})^2, \tag{2-25}$$

with

$$B_{\rm OV} = 7.8\times10^{13}\left(\frac{\mu g_2\cos\alpha}{Z\mathcal{G}E_1\sin^2\theta_{\rm kB}}\right)^{1/4}\left(\frac{f}{T_6^{1/8}}\right)\,{\rm G}, \tag{2-26}$$

where $\mu = A/(1+Z)$ is the "molecular" weight, g_2 is the surface gravity in units of 2×10^{14} cm s^{-2}, T_6 is the surface temperature in units of 10^6 K, and $\mathcal{G} = 1-\exp(-E/kT)$.

Illustrations of different spectral behaviors of polarized soft X-rays from magnetars with different magnetic-field strengths are shown in Figures 2-1 and 2-2. For magnetars with surface magnetic fields satisfying $B \lesssim B_{\rm OV}$, the vacuum resonance lies at a lower density than $\rho_{\rm O-mode}$; the emergent radiation is dominated by the X-mode for $E \lesssim E_{\rm ad}$ and by the O-mode for $E \gtrsim E_{\rm ad}$, i.e., there is a 90° rotation of the polarization angle between $E \lesssim E_{\rm ad}$ and $E \gtrsim E_{\rm ad}$. On the other hand, for $B \gtrsim B_{\rm OV}$, the vacuum resonance lies between $\rho_{\rm O-mode}$ and $\rho_{\rm X-mode}$, and the emergent radiation from the surface is dominated by the X-mode for all values of E.

Quantitative calculations of the atmospheric emission (spectrum and polarization) are fully described in previous works [e.g., 18, 26, 50]. In this paper, since our focus is on the effect of magnetospheric scattering, we adopt a simple prescription for the surface emission. For a given spot (located at the polar angles θ_s, ϕ_s) with temperature T_s, the

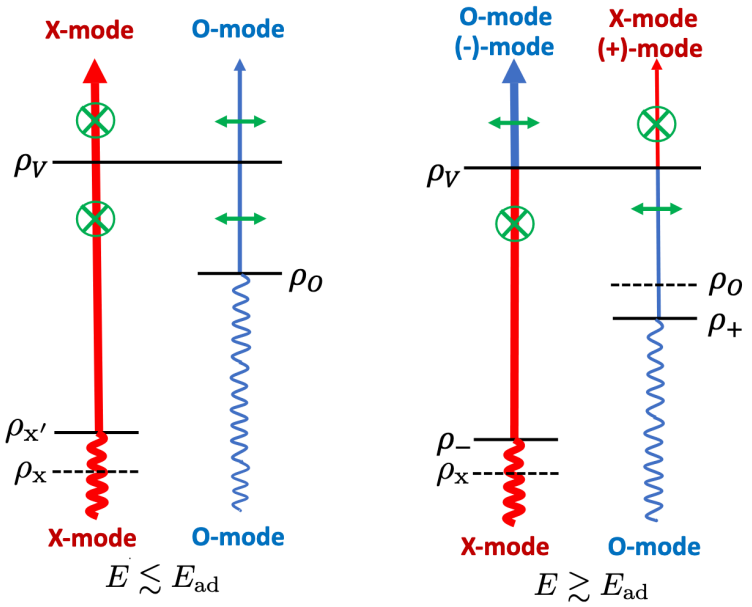

Figure 2-1 Schematic illustration of how vacuum resonance affects the polarization angle of observed polarized X-rays from a magnetar with surface dipole field $B \lesssim B_{\rm QV}$. The resonance layer lies above both the X-mode and O-mode photospheres. For $E \lesssim E_{\rm ad}$, photons evolve non-adiabatically across the resonant layer; thus, the emergent radiation is X-mode-dominated. For $E \gtrsim E_{\rm ad}$, mode conversion is efficient across the resonant layer; thus, the emergent radiation is O-mode-dominated.

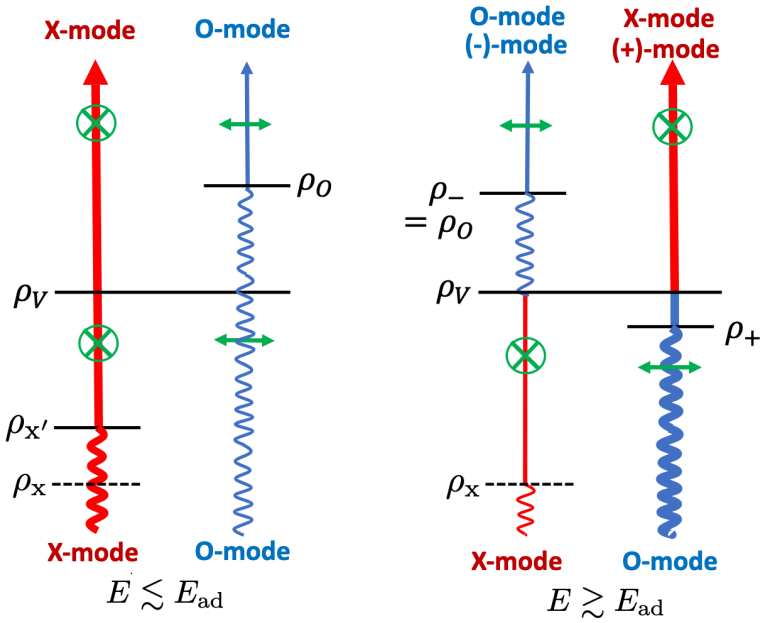

Figure 2-2 Same as Figure 2-1, but with a surface dipole field $B \gtrsim B_{\rm QV}$. The resonant layer lies between the X-mode and O-mode photospheres. In this regime, the emergent radiation is always dominated by the X-mode for all values of E.

total radiative intensity (in the stellar frame) is given by

$$I_{\omega}^{(\mathrm{tot})}(\widehat{\Omega}) = I_{\omega}^{1}(\widehat{\Omega}) + I_{\omega}^{2}(\widehat{\Omega}) \propto \frac{\mu_s^{a-1}\omega^3}{\exp(\hbar\omega/kT_s)-1}, \tag{2-27}$$

where μ_s is the (stellar-frame) cosine between the emission direction ($\widehat{\Omega}$) and the local magnetic field, and $a \geq 1$ is a beaming parameter (we adopt $a = 1$ for isotropic emission). As discussed above, for $B \lesssim B_{\mathrm{QV}}$, the X-ray polarization degree is set to 1 at lower energies (i.e., X-mode-dominated) and to -1 at higher energies (i.e., O-mode-dominated) by comparing E with E_{ad}, using a smoothed transition (e.g., a Fermi–Dirac-type switch). For the numerical calculations in this work, the fractions of the X- and O-mode components, f_{X} and f_{O}, are given by

$$\begin{aligned} f_{\mathrm{O}} &= \left\{1+\exp\left[-6\left(\frac{\hbar\omega}{1\ \mathrm{keV}}-4.0\right)\right]\right\}^{-1}, \\ f_{\mathrm{X}} &= \left\{1+\exp\left[\ 6\left(\frac{\hbar\omega}{1\ \mathrm{keV}}-4.0\right)\right]\right\}^{-1}. \end{aligned} \tag{2-28}$$

2.2.3 General-relativistic effects

To describe photon propagation from the NS surface to the scattering region, general-relativistic effects must be considered. For typical magnetar spin periods $P = 2\pi/\Omega = 2$–12 s, rotational frame-dragging is negligible: $(R\Omega/c)^2 \lesssim 4\times10^{-8}R_6^2P_1^{-2}$ [11]. Thus, the Schwarzschild metric suffices.

Key GR effects include gravitational redshift and light bending. As photons travel to $\gtrsim 10R$ where resonant scattering occurs (see below), the metric at the scattering point is almost flat, with $GM/(10Rc^2) \ll 1$. For redshift, since the photon occupation number $\mathcal{N}(\omega) \propto I_\omega/\omega^3$ is Lorentz invariant, under the redshift $\omega \to g\omega$ where $g = \left[1-2GM/(Rc^2)\right]^{1/2}$ the intensity transforms as $I_\omega \to g^3 I_\omega$.

We treat the light-bending effect using the mapping between local emission angle α and asymptotic angle ψ as in [53], which is accurate for $R \gtrsim 4GM/c^2$ (see Figure 2-3). The approximate relation is given by

$$1-\cos\alpha = (1-\cos\psi)\left(1-\frac{r_g}{R}\right), \tag{2-29}$$

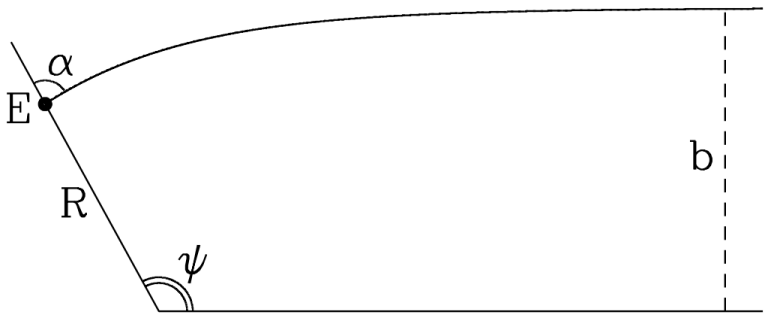

Figure 2-3 Illustration of a photon trajectory, emission angle α, and asymptotic angle ψ. The emission spot is denoted by "E" in the figure. The emission angle is the angle between the initial photon propagation direction and the surface normal. The asymptotic angle ψ denotes the angle between the photon propagation direction at a very large distance and the surface normal at the emission spot.

where $r_g = 2GM/c^2$ is the gravitational radius. When treating the radiative transfer of photons in the magnetosphere, Eq. (2-29) serves as a transformation for the "effective projection" of the emission hot-spot area due to GR light bending.

2.3 Resonant Compton scattering formalism

In the outer magnetosphere, photons are scattered by electrons mainly through RCS. For a magnetar with dipole field $B_{\rm p}$ and twist parameter ξ_τ (see Eq. (2-5)), RCS occurs at the radius (neglecting the motion of electrons; see below)

$$r_{\rm sc} = 10.5\, R \left(\frac{B_{\rm p}}{10^{14}\ {\rm G}}\right)^{1/3} \left(\frac{E}{1\ {\rm keV}}\right)^{-1/3} F(\theta), \tag{2-30}$$

where $F(\theta) = \left(1 - \frac{3}{4}\sin^2\theta\right)^{1/6}$. Given that the Landau level lifetime of gyrating electrons is much shorter than the cyclotron period [11], $\tau_L = (3/4)(\hbar/[\alpha m_e c^2])(B_{\rm Q}/B)^2 \simeq 3 \times 10^{-14} B_{11}^{-2}$ s, electrons can be assumed to remain in the ground state, rendering individual scattering events effectively elastic in the electron rest frame (ERF). We neglect non-resonant scattering and recoil in this work.

2.3.1 Cross sections

In the Thomson limit, the non-relativistic RCS cross sections were first derived by Ventura [54] [see also Chapter 4 of 55]. We denote the unit vector along the propagation

direction by $\widehat{\Omega}$, and the polarization states by $\alpha \in \{1,2\} = \{\mathrm{O},\mathrm{X}\}$. In the ERF, the differential cross section takes the form [e.g., 34]:

$$\left(\frac{\mathrm{d}\sigma}{\mathrm{d}\Omega}\right)^{(\mathrm{ERF})}_{\alpha\widehat{\Omega}'\to\beta\widehat{\Omega}} = \left(\frac{e^2}{m_e c}\right) K'_{\alpha\beta}\ \delta(\omega-\omega_B), \tag{2-31}$$

where $\omega = E/\hbar$ is the photon frequency, $\omega_B = eB/m_e c$ is the electron cyclotron frequency, and the coefficients $K_{\alpha\beta}$ are

$$\begin{aligned} K'_{11} &= \frac{3\pi}{8}\left(\widehat{\Omega}'\cdot\widehat{\mathbf{B}}\right)^2\left(\widehat{\Omega}\cdot\widehat{\mathbf{B}}\right)^2, \\ K'_{12} &= \frac{3\pi}{8}\left(\widehat{\Omega}'\cdot\widehat{\mathbf{B}}\right)^2, \\ K'_{21} &= \frac{3\pi}{8}\left(\widehat{\Omega}\cdot\widehat{\mathbf{B}}\right)^2, \\ K'_{22} &= \frac{3\pi}{8}. \end{aligned} \tag{2-32}$$

Note that all coefficients involving dot products of unit vectors should be calculated in the ERF, so they are all related to the variable β_e. Specifically, all coefficients contain factors of the form $\cos^2\theta_{kB}$, where θ_{kB} denotes the angle between the photon propagation direction $\mathbf{k}$ and the magnetic-field direction $\mathbf{B}$. Due to the relativistic transformation, the projection factors in the NS frame and in the ERF satisfy

$$\cos^2\theta_{kB}^{(\mathrm{ERF})} = \frac{\cos^2\theta_{kB}^{(\mathrm{NS})}}{1-\beta_e^2+\beta^2\cos^2\theta_{kB}^{(\mathrm{NS})}} \tag{2-33}$$

When transforming to the stellar frame, relativistic beaming also modifies the differential cross section:

$$\begin{aligned} \left(\frac{\mathrm{d}\sigma}{\mathrm{d}\Omega}\right)^{(\mathrm{NS})} &= \left(\frac{\mathrm{d}\sigma}{\mathrm{d}\Omega}\right)^{(\mathrm{ERF})}\cdot\frac{\mathrm{d}\Omega_{\mathrm{ERF}}}{\mathrm{d}\Omega_{\mathrm{NS}}} \\ &= \frac{1}{\gamma_e^2(1-\beta_e\mu)^2}\left(\frac{\mathrm{d}\sigma}{\mathrm{d}\Omega}\right)^{(\mathrm{ERF})}, \end{aligned} \tag{2-34}$$

where $\mu = \widehat{\Omega}\cdot\widehat{\mathbf{B}}$ is measured in the NS frame, and the delta function must also transform

$$\delta(\omega-\omega_B)^{(\mathrm{ERF})} \to \frac{1}{\gamma_e(1-\beta_e\mu)}\delta(\omega-\omega_D)^{(\mathrm{NS})}, \tag{2-35}$$

with $\omega_D = \omega_B/[\gamma_e(1-\beta_e\mu)]$ to match the resonant condition in the ERF while preserving the normalization of the delta function. We denote the differential cross section in the stellar frame as

$$\left(\frac{\mathrm{d}\sigma}{\mathrm{d}\Omega}\right)^{(\mathrm{NS})}_{\alpha\widehat{\Omega}'\to\beta\widehat{\Omega}} = \left(\frac{e^2}{m_e c}\right)\, K_{\alpha\beta}\ \delta(\omega-\omega_D) \tag{2-36}$$

with $K_{\alpha\beta} \equiv K'_{\alpha\beta}/[\gamma_e(1-\beta_e\mu)]^3$. The scattering radius for a photon of frequency ω can be determined by solving the resonance condition $\omega = \omega_D$ for a given emission direction and magnetosphere parameters. For the non-relativistic cases with a dipole field, solving $\omega = \omega_D \simeq \omega_B$ yields Eq. (2-30).

In the ERF, integrating (2-31) over scattered directions and summing over β gives the total cross section $\sigma_\alpha(\widehat{\Omega},\beta_e)$ for photons of mode α propagating along $\widehat{\Omega}$, which is also Lorentz-invariant:

$$\begin{aligned}\sigma_1 &= \frac{2\pi^2e^2}{m_e c}\left(\widehat{\Omega}\cdot\widehat{\mathbf{B}}\right)^2\delta(\omega-\omega_B),\\ \sigma_2 &= \frac{2\pi^2e^2}{m_e c}\,\delta(\omega-\omega_B).\end{aligned} \tag{2-37}$$

Using the estimate $\sigma \simeq (\pi^2e^2/m_e c)\,\delta(\omega-\omega_B)$ and Eq. (2-6) for n_e, we obtain the characteristic optical depth across the resonant layer [see also 14]:

$$\tau_0(\widehat{\Omega}) \equiv \int \mathrm{d}s\, n_e\sigma \simeq \frac{\pi\xi_\tau}{4\beta_0}\frac{B}{r_{\mathrm{sc}}}\left|\frac{\mathrm{d}B}{\mathrm{d}s}\right|^{-1} \sim \frac{\pi\xi_\tau}{4\beta_0} \tag{2-38}$$

is of order unity, where ds is integrated across the RCS layer along $\widehat{\Omega}$ and $\left|\frac{\mathrm{d}B}{\mathrm{d}s}\right| = (\widehat{\Omega}\cdot\nabla)B \sim B/r_{\mathrm{sc}}$ is the directional derivative of B along the photon path, both measured in the NS frame.

We note that the optical depth is independent of energy. For a specific polarization mode α, the corresponding optical depth is

$$\tau_\alpha(\widehat{\Omega}) \equiv \int \mathrm{d}s\,\mathrm{d}\beta_e\, n_e f_1(\beta_e)(1-\beta_e\mu)\sigma_\alpha, \tag{2-39}$$

where the factor $(1-\beta_e\mu)$ reflects the encounter rate between photons and electrons due to their relative motion in the NS frame. Note that the estimated $\tau_\alpha \sim 1$ indicates that each emergent photon is expected to be scattered once on average in the magnetosphere.

2.3.2 Polarized radiative transfer in magnetosphere

Adiabatic polarization evolution during propagation. After a photon leaves the NS surface, it propagates in the magnetosphere, whose dielectric property is dominated by vacuum polarization [56]. At small radii, the photon's polarization state evolves adiabatically following the varying magnetic field it experiences, such that the specific mode intensity is constant (except for the GR corrections discussed in Section 2.2.3) [1]. To illustrate this physical property, we begin with the wave equation of an electromagnetic wave with a given frequency:

$$\nabla \times (\mu' \cdot \nabla \times \mathbf{E}) = \frac{\omega^2}{c^2}\varepsilon \cdot \mathbf{E}. \tag{2-40}$$

Assuming that the medium is only weakly anisotropic so that the propagation trajectory of the electromagnetic wave is not significantly deflected, we further assume a plane-wave solution of the form $\mathbf{E} = \mathbf{E}_0(z)e^{-\mathrm{i}\omega t} = \mathbf{A}(z)e^{\mathrm{i}(k_0 z-\omega t)}$, where $\mathbf{A}(z)$ is the photon polarization vector. Under appropriate approximations, the above equation can be reduced to the simpler form

$$\begin{aligned}
\frac{\mathrm{d}A_x}{\mathrm{d}z} &= \frac{\mathrm{i}k_0\delta}{2}[MA_x + PA_y], \\
\frac{\mathrm{d}A_y}{\mathrm{d}z} &= \frac{\mathrm{i}k_0\delta}{2}[PA_x + NA_y], \\
A_z &= -\frac{\varepsilon_{zx}}{\varepsilon_{zz}}A_x - \frac{\varepsilon_{zy}}{\varepsilon_{zz}}A_y.
\end{aligned} \tag{2-41}$$

[1] An exception occurs when the photon encounters the quasi-tangential (QT) point, where the photon momentum is nearly aligned with the local magnetic field. The X-ray polarization may change significantly when the photon passes through the QT region [57]. Since only a small fraction of the NS surface radiation is affected by the quasi-tangential propagation, we shall neglect this effect in this paper.

In the above equations, the dimensionless parameters M,N,P depend on the components of the permeability tensor and the direction vector of the external magnetic field [23]:

$$\begin{aligned} M &= \frac{(7\widehat{B}_x^2+4\widehat{B}_y^2)\mu'_{xx}-12\delta\widehat{B}_x^2\widehat{B}_y^2}{\mu'_{xx}\mu'_{yy}-16\delta^2\widehat{B}_x^2\widehat{B}_y^2}, \\ N &= \frac{(4\widehat{B}_x^2+7\widehat{B}_y^2)\mu'_{yy}-12\delta\widehat{B}_x^2\widehat{B}_y^2}{\mu'_{xx}\mu'_{yy}-16\delta^2\widehat{B}_x^2\widehat{B}_y^2}, \\ P &= \frac{[3\mu'_{xx}-4\delta(7\widehat{B}_y^2+4\widehat{B}_x^2)]\widehat{B}_x\widehat{B}_y}{\mu'_{xx}\mu'_{yy}-16\delta^2\widehat{B}_x^2\widehat{B}_y^2}. \end{aligned} \tag{2-42}$$

Under the weak-field approximation, QED effects modify the polarization vector of an electromagnetic wave propagating in vacuum. The characteristic propagation length scale over which significant evolution occurs is

$$\ell_1 = \frac{2}{k_0\delta} \simeq 130\left(\frac{B}{10^{11}\ \mathrm{G}}\right)^{-2}\left(\frac{E}{1\ \mathrm{keV}}\right)^{-1}\ \mathrm{cm}, \tag{2-43}$$

Meanwhile, in a dipole field, the spatial scale over which the magnetic-field strength varies significantly is

$$\ell_2 = \frac{B}{|\hat{r}\cdot\nabla B|} = \frac{r}{3}. \tag{2-44}$$

Near the stellar surface, $\ell_1 \ll \ell_2$, and the wave-vector evolution is in the adiabatic regime: the photon always evolves with the local magnetic-field direction as its polarization reference direction and preserves its polarization state along the trajectory until resonant Compton scattering occurs at $r_{\rm sc}$ in the magnetosphere. After being scattered there, the photon continues to propagate. Far from the star, $\ell_1 \gg \ell_2$, which corresponds to the regime in which the photon polarization state in the stellar frame no longer follows the local magnetic field on the magnetic-field variation scale. There is a transition region between "adiabatic evolution of the photon polarization vector along the magnetic-field direction" and "decoupling of the polarization from the magnetic field". We use $\ell_1 \simeq \ell_2$ to determine the corresponding magnetar radius scale $r_{\rm pl}$, namely the polarization-limiting radius; beyond this radius, the photon polarization vector decouples from the magnetic

field. The value of $r_{\rm pl}$ can be estimated as

$$r_{\rm pl} = 4.8 \left(\frac{B_{\rm p}}{10^{11}\ {\rm G}}\right)^{2/5} \left(\frac{E}{1\ {\rm keV}}\right)^{1/5} \left(\frac{R_{\rm NS}}{10\ {\rm km}}\right)^{1/5} R. \tag{2-45}$$

For typical magnetar parameters, the polarization-limiting radius is approximately $\gtrsim 100R$. For all rays emitted from a magnetar and reaching the observer, although they have some transverse separation, they can be approximately regarded as experiencing the same uniform magnetic-field environment when they arrive at the polarization-limiting radius. The corresponding polarization vectors can therefore be added nearly collinearly, rather than canceling because of random orientations, thereby increasing the polarization degree of the final observed signal. Based on this mechanism, the very high linear polarization degrees in recently accumulated IXPE data are usually regarded as important observational evidence for QED vacuum polarization effects [e.g., 58, 59].

Radiative transfer during the scattering process. Near the RCS layer, the transfer equation for polarized intensity $I^{\alpha}_{\omega}(\widehat{\Omega}) \equiv I^{\alpha}_{\omega}(\widehat{\Omega}, \mathbf{r}_{\rm sc})$ (where the $\mathbf{r}_{\rm sc}$ dependence highlights the dependence on the scattering location) of mode α and frequency ω is given by (in the NS frame)

$$\begin{aligned}\left(\widehat{\Omega}\cdot\nabla\right) I^{\alpha}_{\omega}(\widehat{\Omega}) = &-\int {\rm d}\beta_e\, n_e f_1(\beta_e)(1-\beta_e\mu)\sigma_{\alpha}(\widehat{\Omega},\beta_e) I^{\alpha}_{\omega}(\widehat{\Omega}) \\ &+\sum_{\beta}\int {\rm d}\beta_e \oint {\rm d}\Omega'\, n_e f_1(\beta_e)(1-\beta_e\mu'_0)\,\eta^{-3} I^{\beta}_{\eta\omega}(\widehat{\Omega}') \left(\frac{{\rm d}\sigma}{{\rm d}\Omega'}\right)^{\rm (NS)}_{\beta\widehat{\Omega}'\to\alpha\widehat{\Omega}},\end{aligned} \tag{2-46}$$

where $\mu'_0 = \widehat{\Omega}'\cdot\hat{B}$ is measured in the NS frame, $\eta = \eta(\beta_e, \widehat{B}, \widehat{\Omega}', \widehat{\Omega}) = (1-\beta_e^2)/[\ (1-\beta_e\cos\theta_1)(1+\beta_e\cos\theta'_2)\ ]$ is the Doppler-shift factor linking the incident ($\eta\omega$) and scattered (ω) frequencies, $\cos\theta_1 = \widehat{\Omega}'\cdot\widehat{B}$ and $\cos\theta'_2 = \widehat{\Omega}\cdot\widehat{B}$ are calculated in the NS frame and ERF, respectively, and the η^{-3} factor represents the Doppler intensity rescaling through scattering (i.e., Comptonization). Note also that the factors $(1-\beta_e\mu)$ and $(1-\beta_e\mu'_0)$ in Eq. (2-46) reflect the encounter rate due to relative motion.

We denote the position vector of a small emission patch on the NS surface by $R\widehat{\Omega}_s$ and the position vector of the scattering location by $\mathbf{r}_{\rm sc} = r_{\rm sc}\widehat{\Omega}_0$. Then the incoming direction vector can be calculated as $\widehat{\Omega}' = (r_{\rm sc}\widehat{\Omega}_0 - R\widehat{\Omega}_s)/|r_{\rm sc}\widehat{\Omega}_0 - R\widehat{\Omega}_s|$. The first term

on the RHS of Eq. (2-46) represents the attenuation of the incoming intensity along $\widehat{\Omega}$, and the second term represents the scattered-in contribution. For non-relativistic electrons ($\beta_e \ll 1$), given the narrowness of the resonance, the scattering occurs on a thin surface. For single scattering, Eq. (2-46) can be solved to yield the relationship between the incoming (before RCS) intensity $I^{\alpha}_{\omega,\text{in}}$ and the outgoing (after RCS) intensity $I^{\alpha}_{\omega,\text{out}}$ as

$$I^{\alpha}_{\omega,\text{out}}(\widehat{\Omega}) = I^{\alpha\ (\text{I})}_{\omega,\text{out}}(\widehat{\Omega}) + I^{\alpha\ (\text{II})}_{\omega,\text{out}}(\widehat{\Omega}). \tag{2-47}$$

The first term is the attenuated incoming intensity that propagates along $\widehat{\Omega}$:

$$I^{\alpha\ (\text{I})}_{\omega,\text{out}}(\Omega) = I^{\alpha}_{\omega,\text{in}}(\widehat{\Omega}) \exp\left(-\tau_{\alpha}\right), \tag{2-48}$$

where $\tau_{\alpha}(\widehat{\Omega}) = \int \mathrm{d}s\, \mathrm{d}\beta_e\, n_e f_1(\beta_e)(1-\beta_e\mu)\sigma_{\alpha}$. The second term in Eq. (2-47) represents the scattered-in part, which is given by

$$\begin{aligned} I^{\alpha\ (\text{II})}_{\omega,\text{out}}(\widehat{\Omega}) = & \sum_{\beta} \int \mathrm{d}s\, \mathrm{d}\beta_e \oint \mathrm{d}\Omega'\, n_e f_1(\beta_e) \\ & \times (1-\beta_e\mu)\eta^{-3} I^{\beta}_{\eta\omega,\text{in}}(\widehat{\Omega})' \left(\frac{\mathrm{d}\sigma}{\mathrm{d}\Omega'}\right)^{(\text{NS})}_{\beta\widehat{\Omega}'\to\alpha\widehat{\Omega}}. \end{aligned} \tag{2-49}$$

In Eq. (2-49), the integration over ds can be simplified using the delta function in the cross section, and the integration over dΩ' for a given scattering site $\mathbf{r}_{\text{sc}}$ can be written as

$$\oint \mathrm{d}\Omega' = \oint \frac{\mathrm{d}\mathbf{A}_s \cdot \widehat{\Omega}'}{\left|\mathbf{r}_{\text{sc}} - R\widehat{\Omega}_s\right|^2} = \int \frac{\mathrm{d}A_s \left(\widehat{\Omega}_s \cdot \widehat{\Omega}'\right)}{\left|\mathbf{r}_{\text{sc}} - R\widehat{\Omega}_s\right|^2} \Theta\left(\widehat{\Omega}_s \cdot \widehat{\Omega}'\right), \tag{2-50}$$

where $\mathrm{d}\mathbf{A}_s = \widehat{\Omega}_s \mathrm{d}A_s$ is the surface-element vector of the emission spot on the NS surface (see Figure 2-4). Note that we have included a Heaviside function $\Theta\left(\widehat{\Omega}_s \cdot \widehat{\Omega}'\right)$ to ensure that only photons emitted outward from the surface are accounted for. Substituting the expression of n_e and $(\mathrm{d}\sigma/\mathrm{d}\Omega')$ with the simplifications above, Eq. (2-49) can be rewritten

as

$$I^{\alpha\ (\mathrm{II})}_{\omega,\mathrm{out}}(\widehat{\Omega}) = \int \frac{\mathrm{d}A_s \left(\widehat{\Omega}_s\cdot\widehat{\Omega}'\right)\Theta\left(\widehat{\Omega}_s\cdot\widehat{\Omega}'\right)}{4\pi\left|\mathbf{r}_{\mathrm{sc}} - R\widehat{\Omega}_s\right|^2}\frac{\xi_\tau}{\beta_0}\sum_\beta\int \mathrm{d}\beta_e\ f_1(\beta_e)(1-\beta_e\mu_0') \\ \times\eta^{-3}I^\beta_{\eta\omega,\mathrm{in}}(\widehat{\Omega}')K_{\beta\alpha}(\widehat{\Omega}'\to\widehat{\Omega})\frac{B}{r_{\mathrm{sc}}}\left|\frac{\partial}{\partial s}\left[\frac{B}{\gamma_e(1-\beta_e\mu)}\right]\right|^{-1}, \tag{2-51}$$

where $K_{\beta\alpha}(\widehat{\Omega}'\to\widehat{\Omega})$ is given by Eq. (2-36). Eqs. (2-47), (2-48), and (2-51) give the total outgoing intensity after one scattering. We expect that the single-scattering approximation is valid when $\tau_\alpha \lesssim 1$. We may still apply it for the $\tau_\alpha \gtrsim 1$ cases to show qualitative physical trends. Higher-order solutions can be obtained perturbatively, analogous to those in [32], where an analytical solution for the one-dimensional case is given.

To calculate the factor $|\partial/\partial s\ [B/\gamma_e(1-\beta_e\mu)]|^{-1}$ in Eq. (2-51), we should use the product rule for differentiation:

$$\frac{\partial}{\partial s}\left[\frac{B}{\gamma_e(1-\beta_e\mu)}\right] = \frac{1}{\gamma_e(1-\beta_e\mu)}\frac{\partial B}{\partial s} + \frac{\beta_e}{\gamma_e(1-\beta_e\mu)^2}\frac{\partial}{\partial s}(\widehat{\Omega}\cdot\hat{B}), \tag{2-52}$$

the first term involving $\partial B/\partial s$ can be calculated with ease. To derive $\partial/\partial s\ (\widehat{\Omega}\cdot\hat{B})$ in the second term, we begin by calculating the directional derivative in a spherical coordinate system:

$$r\frac{\partial}{\partial s} = \widehat{\Omega}\cdot\hat{\theta}_0\frac{\partial}{\partial\theta_0} + \frac{\widehat{\Omega}\cdot\hat{\phi}_0}{\sin\theta_0}\frac{\partial}{\partial\phi_0}, \tag{2-53}$$

where θ_0, ϕ_0 represent the spherical coordinates. Since $\widehat{\Omega}$ and $\hat{B}$ are known according to the physical setup, in the Cartesian coordinates shown in Figure 2-4 (see below), we have

$$\widehat{\Omega} = (0, \sin\theta, \cos\theta) \tag{2-54}$$

and

$$\hat{B} = \frac{1}{(1+\xi_\tau^2)^{1/2}}(3\cos\theta_0\sin\theta_0\cos\phi_0 - \beta_1\sin\theta_0\sin\phi_0, \\ 3\cos\theta_0\sin\theta_0\sin\phi_0 + \beta_1\sin\theta_0\cos\phi_0, \\ 3\cos^2\theta_0 - 1). \tag{2-55}$$

By substituting the equations above and the expression for the unit vectors $\hat{\theta}_0, \hat{\phi}_0$ into Eq. (2-53), we are finally able to obtain the correct expression for the directional derivative factor $|\partial/\partial s\ [B/\gamma_e(1-\beta_e\mu)]|$.

After RCS, an outgoing photon continues to propagate in the magnetosphere, with its polarization state evolving adiabatically, i.e., $I^{\alpha}_{\omega}(\widehat{\Omega}) = \text{constant}$. Eventually, the photon reaches the "polarization-limiting radius" $r_{\rm pl}$, beyond which the polarization state is frozen. The value of $r_{\rm pl}$ depends on the photon energy E, the dipole field strength $B_{\rm p}$, and the magnetar rotation rate, and generally $r_{\rm pl}/R \gtrsim 100$ [18]. Since $r_{\rm pl} \gg r_{\rm sc}$, regardless of the structure and shape of the RCS layer, the radiation emerging from the layer with mode intensities I^{α}_{ω} evolves adiabatically in the magnetosphere such that the radiation at $r > r_{\rm pl}$ consists of approximately the same X-mode and O-mode intensities as those emerging from the RCS layer, with a small mixture of circular polarization generated around $r_{\rm pl}$. See [26] for more details.

2.4 Computational workflow

In our magnetar radiation model, different physical processes are separated cleanly by their characteristic radial scales: emission near the surface, propagation and scattering through the magnetosphere, and polarization evolution from the scattering layer to the polarization-limiting radius. Our calculations are divided into three steps:

1. *Emission near the surface under vacuum resonance*: Near the neutron star surface and atmosphere, the dominant process is polarized X-ray emission influenced by QED vacuum resonance. This region has been extensively studied [e.g., 18, 26, 27], allowing us to directly adopt previously computed emissivity profiles as input. In this work, we use a simplified prescription for the surface emission, as described in Section 2.2.2.

2. *Adiabatic propagation from the surface and RCS*: As discussed, resonant scattering occurs at $\sim 10R$. After emission from the NS surface, the photon polarization evolves adiabatically following the magnetic field and propagates solely under gravitational effects until scattering. Light bending is handled using the method of [53]. Specifically, the light-bending mapping between local emission angle α and asymptotic angle ψ corresponds to a mapping between $\left(\widehat{\Omega}_s \cdot \widehat{\Omega}'\right)$ at the RCS layer

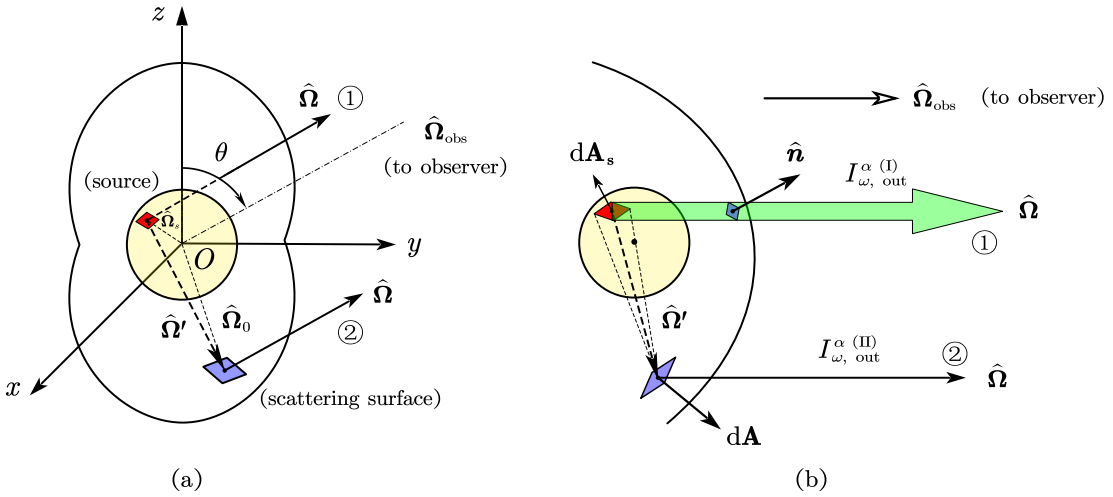

Figure 2-4 Schematic illustration of the radiative transfer with resonant Compton scattering and the computation of the observed polarization flux. The surface element of the NS is $d\mathbf{A}_s = \widehat{\Omega}_s dA_s$. The scattering surface element (located at $\mathbf{r}_{\rm sc} = r_{\rm sc}\widehat{\Omega}_{\rm sc}$) is denoted by dA. The scattered radiation propagates along the direction $\widehat{\Omega} \simeq \widehat{\Omega}_{\rm obs}$, and the incident radiation (before scattering) propagates along $\widehat{\Omega}' = (r_{\rm sc}\widehat{\Omega}_0 - R\widehat{\Omega}_s)/|r_{\rm sc}\widehat{\Omega}_0 - R\widehat{\Omega}_s|$. The magnetic axis of the magnetar is along the z-axis, and $\widehat{\Omega}_{\rm obs}$ is in the yz plane, with the angle between $\widehat{\Omega}_{\rm obs}$ and the z-axis being θ.

and that at the NS surface, which is used in Eq. (2-51). Note that the dot product in Eq. (2-51) represents the cosine of the asymptotic angle after light bending. We shall see later that this mapping is also applied in calculating the flux contribution of $I^{\alpha\ (\rm I)}_{\omega,\rm out}$, where a similar dot product also appears.

3. *Continuing adiabatic propagation to large distances where polarization freezes*: After scattering, the polarization continues to evolve adiabatically until the photon reaches the polarization-limiting radius ($\gg r_{\rm sc}$), where the polarization freezes and aligns coherently, yielding the observable net polarization. The observed flux is computed by integrating the contributions from all locations on the scattering surface. Specifically, we integrate the mode-resolved intensity $I^{\alpha}_{{\rm out},\omega}\left(\widehat{\Omega}, \mathbf{r}_{\rm sc}(\widehat{\Omega}_0)\right)$ over the outer surface of the scattering layer.

Figure 2-4 illustrates the geometric framework for our calculations of the magnetar X-ray radiation. Panel (a) defines the geometry: we set up a Cartesian coordinate system with the magnetic axis along the z-axis, and the observer's line of sight (LOS) is in the yz

plane at angle θ from the z-axis. The radiation source (position vector $R\widehat{\Omega}_s$) is located at (θ_s, ϕ_s) on the NS surface. The location on the scattering surface is denoted by $\mathbf{r}_{\rm sc} = r_{\rm sc}\widehat{\Omega}_0$. The direction of the incoming photon is $\widehat{\Omega}'$, and that of the scattered photon is $\widehat{\blacksquare}$. Two photon populations contribute to the observed flux, as discussed in Section 2.3.2 and illustrated in Figure 2-4:

- *Attenuation term* $I^{\alpha\ (\rm I)}_{\omega,\rm out}(\widehat{\Omega})$ — photons emitted directly toward the observer, attenuated by scattering;
- *Scattered-in term* $I^{\alpha\ (\rm II)}_{\omega,\rm out}(\widehat{\Omega})$ — photons from all other directions scattered into the LOS.

Panel (b) of Figure 2-4 shows how scattered rays reach the observer. Ignoring stellar surface occultation, the total polarized flux in mode α is given by

$$\mathcal{F}^{\alpha}_{\omega} = \mathcal{F}^{\alpha\ (\rm I)}_{\omega} + \mathcal{F}^{\alpha\ (\rm II)}_{\omega} = \int I^{\alpha}_{\omega,\rm out}(\widehat{\Omega}) \left(\widehat{\Omega}\cdot\widehat{\Omega}_{\rm obs}\right) {\rm d}\Omega. \tag{2-56}$$

Since the rays reaching the observer from different locations on the scattering surface are nearly parallel, we have $\left(\widehat{\Omega}\cdot\widehat{\Omega}_{\rm obs}\right) = 1$. Substituting Eqs. (2-47), (2-48), and (2-51) into Eq. (2-56), using ${\rm d}\Omega = |{\rm d}\mathbf{A}\cdot\widehat{\Omega}_{\rm obs}|/D^2$ with ${\rm d}\mathbf{A}$ being the area-element vector of the scattering surface and D being the distance to the observer, we obtain

$$\begin{aligned}
\mathcal{F}^{\alpha\ (\rm I)}_{\omega} &= \frac{A_s}{D^2}\left(\widehat{\Omega}_s\cdot\widehat{\Omega}_{\rm obs}\right) I^{\alpha}_{\omega,\rm in}(\widehat{\Omega}_{\rm obs})\exp(-\tau_\alpha), \\
\mathcal{F}^{\alpha\ (\rm II)}_{\omega} &= \frac{A_s}{4\pi D^2}\frac{\xi_\tau}{\beta_0}\sum_{\beta}\int {\rm d}\beta_e \oint {\rm d}\Omega_0\ f_1(\beta_e)\eta^{-3} I^{\beta}_{\eta\omega,\rm in}(\widehat{\Omega}') \\
&\quad \times (1-\beta_e\mu')\frac{r_{\rm sc}^2\left|\hat{\mathbf{n}}\cdot\widehat{\Omega}_{\rm obs}\right|}{\left|\mathbf{r}_{\rm sc} - R\widehat{\Omega}_s\right|^2}\left(\widehat{\Omega}_s\cdot\widehat{\Omega}'\right)\Theta\left(\widehat{\Omega}_s\cdot\widehat{\Omega}'\right) \\
&\quad \times K_{\beta\alpha}(\widehat{\Omega}'\to\widehat{\Omega}_{\rm obs})\frac{B}{r_{\rm sc}}\left|\frac{\partial}{\partial s}\left[\frac{B}{\gamma_e(1-\beta_e\mu)}\right]\right|^{-1},
\end{aligned} \tag{2-57}$$

where we have assumed a small emission surface area A_s on the NS surface — in general, an integration over the whole NS surface can be performed. In Eq. (2-57), we have used ${\rm d}\mathbf{A} = \hat{\mathbf{n}}\ r_{\rm sc}^2{\rm d}\Omega_0$, where $\hat{\mathbf{n}}$ is the surface normal vector of the scattering surface. Note that the final form of the first expression in Eq. (2-57) does not involve an integration over

the scattering surface, since only photons emitted directly toward the observer without scattering contribute to this term. Also note that, to simplify notation, the dot products $\left(\widehat{\Omega}_s \cdot \widehat{\Omega}_{\rm obs}\right)$ and $\left(\widehat{\Omega}_s \cdot \widehat{\Omega}'\right)$ in Eq. (2-57) do not include GR effects. As mentioned before, when substituting the incoming intensity $I^{\alpha}_{\omega,\rm in}$, we must account for GR light bending from the NS surface to the scattering layer. In this context, the dot products $\left(\widehat{\Omega}_s \cdot \widehat{\Omega}_{\rm obs}\right)$ and $\left(\widehat{\Omega}_s \cdot \widehat{\Omega}'\right)$ represent the effective projection of the emission area onto the incoming direction $\widehat{\Omega}'$ after light bending. Similarly, by mapping $\left(\widehat{\Omega}_s \cdot \widehat{\Omega}_{\rm obs}\right)$ back to the NS surface using the method of [53], we can incorporate the GR light bending effect in Eq. (2-57).

After we obtain the fluxes $\mathcal{F}^{\alpha}_{\omega}$ of each mode, the linear polarization degree can be calculated as

$$P_{\rm L}(\omega) = \frac{\mathcal{F}^{2}_{\omega} - \mathcal{F}^{1}_{\omega}}{\mathcal{F}^{2}_{\omega} + \mathcal{F}^{1}_{\omega}}. \tag{2-58}$$

By analyzing the spectral dependence of the polarization degree, we can identify the effects of resonant Compton scattering.

2.5 Summary

This chapter has presented the semi-analytical theoretical framework used to calculate polarized soft X-ray radiation from magnetars, taking into account the effects of QED vacuum resonance and magnetospheric resonant Compton scattering on the observed spectropolarimetric signatures. We adopt a simplified parameterized description for the magnetospheric model, represent the magnetar atmospheric radiation including vacuum-resonance effects through an idealized initial input, treat general-relativistic light bending during photon propagation from surface emission to RCS using high-accuracy approximate mapping relations, and handle RCS radiative transfer based on the relativistic radiative transfer equation under the single-scattering approximation. The overall framework has high physical transparency and controllability, allowing the relative strengths of different physical effects to be controlled by varying the model parameters and thereby facilitating multidimensional parameter studies.

3 Results of Simplified Fiducial Model

3.1 Polarized flux from simplified model

To identify how each ingredient in our semi-analytic treatment shapes the observables, we begin with a simplified model for preliminary analysis. Throughout this section, we adopt a pure dipole field with a cold-plasma approximation, ignoring relativistic effects. The electron number density follows Eq. (2-6), with the parameter $\zeta \equiv \xi_\tau/\beta_0$ controlling the electron density (see Eq. (2-6)) and hence the effective RCS strength (see Eq. (2-38)), independently of the field geometry. Under these assumptions, the mode-resolved optical depths can be calculated as $\tau_\alpha^{(\mathrm{NR})} = \int \mathrm{d}s\; n_e \sigma_\alpha^{(\mathrm{NR})}$ and the flux can be simplified to

$$\begin{aligned}
\mathcal{F}_\omega^{\alpha(\mathrm{NR,I})} =& \frac{A_s \widehat{\Omega}_s \cdot \widehat{\Omega}_{\mathrm{obs}}}{D^2} I^\alpha_{\omega,\mathrm{in}}(\widehat{\Omega}_{\mathrm{obs}}) \exp\left(-\tau_\alpha^{(\mathrm{NR})}\right), \\
\mathcal{F}_\omega^{\alpha\ (\mathrm{NR,II})} =& \frac{A_s \zeta}{4\pi D^2} \sum_\beta \oint \mathrm{d}\Omega_0\; K_{\beta\alpha} I^\beta_{\omega,\mathrm{in}}(\widehat{\Omega}')\; \frac{B}{r_{\mathrm{sc}}} \left|\frac{\mathrm{d}B}{\mathrm{d}s}\right|^{-1} \\
& \times \frac{r_{\mathrm{sc}}^2 \left|\hat{\mathbf{n}}\cdot\widehat{\Omega}_{\mathrm{obs}}\right|}{\left|\mathbf{r}_{\mathrm{sc}} - R\widehat{\Omega}_s\right|^2} \left(\widehat{\Omega}_s\cdot\widehat{\Omega}'\right) \Theta\left(\widehat{\Omega}_s\cdot\widehat{\Omega}'\right).
\end{aligned} \tag{3-1}$$

For our fiducial setup, we adopt magnetar parameters $B_{\mathrm{p}} = 10^{14}$ G, $R = 10$ km, and $kT_s = 0.6$ keV, with the emission point located at $(\theta_s, \phi_s) = (65^\circ, 30^\circ)$ and the observer's viewing angle set to $\theta = 25^\circ$. We compute the polarized fluxes and linear polarization degree in the IXPE band (2–8 keV).

Figures 3-1 and 3-2 illustrate the impact of varying ζ on both the mode-resolved spectra and polarization of the observed radiation. For weaker scattering with small ζ (where the single-scattering approximation is valid), the initially dominant mode is attenuated, while the subdominant mode gains power through scattering, reducing the O/X spectral contrast. For stronger scattering with larger ζ, the total flux increases, since the scattered-in term scales directly with electron density. As the density becomes too high, our single-scattering approximation may overestimate the flux. In this regime, the spectral shapes of the O- and X-modes become similar.

Figure 3-2 shows the corresponding linear polarization degree $P_{\mathrm{L}}(\omega)$ as a function

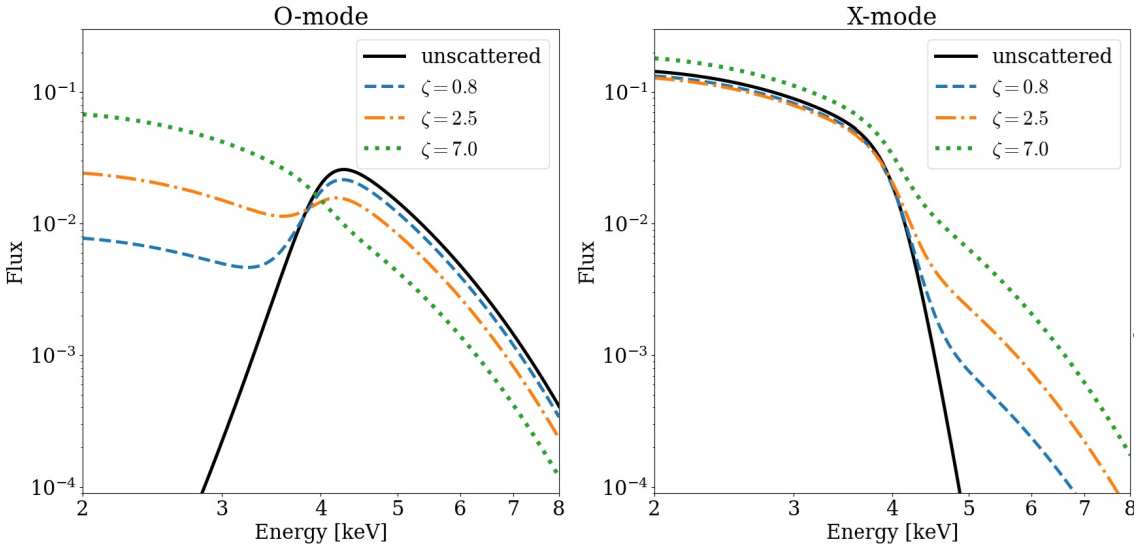

Figure 3-1 The relative O-mode and X-mode flux spectra for different scattering strengths compared to the unscattered case in the simplified setup with $B_{\rm p} = 10^{14}$ G, $kT = 0.6$ keV, $R = 10$ km, a hot spot at $(\theta_s, \phi_s) = (65^\circ, 30^\circ)$, viewing angle $\theta = 25^\circ$, and varying $\zeta \equiv \xi_\tau/\beta_0 = 0.8, 2.5, 7.0$ (see Eqs. (2-6) and (2-38)).

of photon energy. As the RCS strength increases, $P_{\rm L}$ flattens, and it becomes positive for all photon energies in the case of $\zeta = 7$. Thus, the original mode-switching signature may disappear in strong-scattering cases. As we will see later, incorporating special-relativistic effects may erase the mode-switching signature more efficiently, even for cases with low optical depths. This phenomenon will be discussed in more detail in Sections 4 and 5.

Regarding the validity of our calculations, all the results above rely on the assumption of single scattering, i.e., a small resonant optical depth. Our numerical checks confirm that the estimated optical depth (~ 0.1–1) from Section 2 is valid. Specifically, for the geometry used above, we find $\tau \lesssim 1$ when $\zeta \lesssim 3.7$, supporting the accuracy of the single-scattering solution in this range. Notably, the disappearance of the mode switch in our calculations occurs at $\zeta \gtrsim 5.6$, where the single-scattering approximation becomes questionable.

For the scattering results in the high magnetospheric-density regime, or equivalently at large optical depth, the contribution from the scattered-in term is proportional to n_e and may therefore be overestimated at high density, potentially leading to a violation of energy conservation. A direct treatment is to introduce a factor such as $\exp(-\tau_{\alpha,\rm esc})$ to

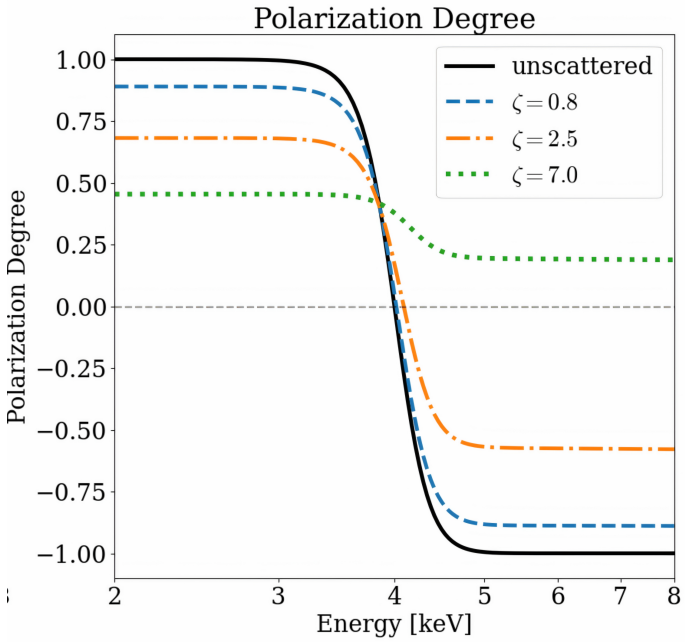

Figure 3-2 The corresponding linear polarization degree $P_L(\omega)$ as a function of energy for different scattering strengths compared to the unscattered case in the simplified setup with $B_{\rm p} = 10^{14}$ G, $kT = 0.6$ keV, $R = 10$ km, a hot spot at $(\theta_s, \phi_s) = (65^\circ, 30^\circ)$, viewing angle $\theta = 25^\circ$, and varying $\zeta \equiv \xi_\tau/\beta_0 = 0.8, 2.5, 7.0$ (see Eqs. (2-6) and (2-38)).

suppress the scattered-in contribution again, where $\tau_{\alpha,\rm esc}$ denotes the optical depth experienced by a photon after RCS as it propagates to infinity, and physically corresponds to the contribution from higher-order terms (we do not include the effect of $\tau_{\rm esc}$ in Section 4). For the present system, in the non-relativistic limit, all scattering occurs on the same geometrical surface; if non-resonant scattering is neglected, one has $\tau_{\alpha,\rm esc} = 0$. To estimate a lower bound on the ability of RCS to erase the mode-switching feature, we further define a limiting-case flux calculated with $\tau_{\alpha,\rm esc} = \tau_\alpha$:

$$\begin{aligned} \mathcal{F}_{\omega,\rm limit}^{\alpha(\rm NR,I)} &= \mathcal{F}_{\omega}^{\alpha(\rm NR,I)}, \\ \mathcal{F}_{\omega,\rm limit}^{\alpha\ (\rm NR,II)} &= \mathcal{F}_{\omega}^{\alpha\ (\rm NR,II)} \exp(-\tau_\alpha). \end{aligned} \tag{3-2}$$

Figure 3-3 shows the limiting case for $\zeta = 7.0$, where $\tau_{\alpha,\rm esc} = 0$ and τ_α are adopted respectively as two limiting-case estimates for calculating the flux and polarization spectra. As shown in the figure, after introducing a larger $\tau_{\alpha,\rm esc}$, the flux in the limiting case is substantially suppressed and therefore does not violate energy conservation. However,

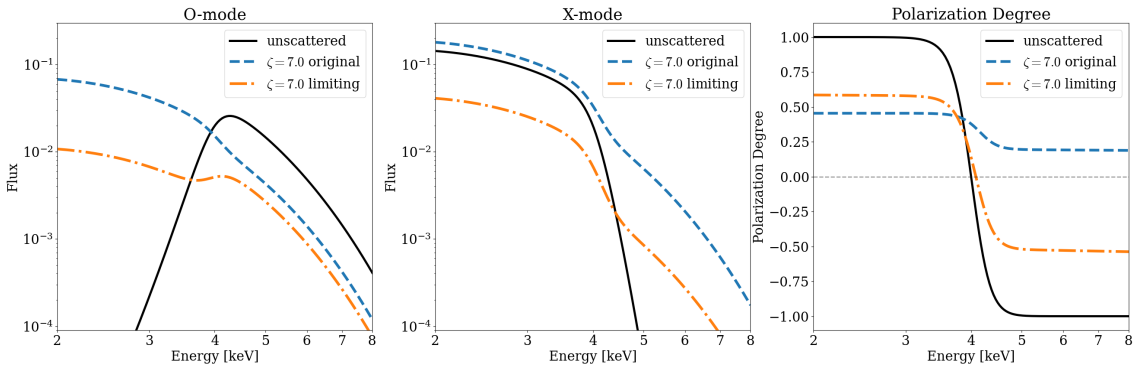

Figure 3-3 The relative O-mode and X-mode flux and polarization spectra for different flux scenarios ($\tau_{\alpha,\mathrm{esc}} = 0$ or τ_α) compared to the unscattered case in the simplified setup with $B_\mathrm{p} = 10^{14}$ G, $kT = 0.6$ keV, $R = 10$ km, a hot spot at $(\theta_s, \phi_s) = (65^\circ, 30^\circ)$, viewing angle $\theta = 25^\circ$, and $\zeta \equiv \xi_\tau/\beta_0 = 7.0$ (see Eqs. (2-6) and (2-38)).

because the scattered-in contribution is also significantly weakened, the behavior originally indicated in the right panel, namely that RCS may erase the mode-switching feature, becomes less evident. In a more realistic situation, the scattered-in contribution should be substantially larger than in this limiting case; nevertheless, the behavior of the polarization degree remains clearly uncertain in the strong-RCS regime. This is precisely why the applicability of the single-scattering approximation at high optical depth was noted above as being "questionable" (for the discussion on the validity of the single-scattering approximation, see Section 4.1).

It is worth noting that in the subsequent full-model study, once relativistic effects are included, RCS can still robustly produce the disappearance of the mode-switching behavior even in cases that generally satisfy $\tau \lesssim 0.4$. This indicates that the richer behavior of magnetar soft X-ray polarization spectra is produced not only by RCS itself, but also by relativistic effects.

3.2 Summary

In this chapter, we construct a simplified magnetar model in the non-relativistic and cold-plasma limits and calculate the polarization spectra of the corresponding observed X-ray signal. By examining this simplified model, we preliminarily identify the main physical effects of RCS and obtain an intuitive understanding of the theoretical validity boundary of the semi-analytical model.

4 Full Model: Parameter Study

In this section, we adopt the full model setup, including both the thermal velocity distribution of magnetospheric electrons and special- and general-relativistic effects. When the electron velocities are thermal about a mean drift, the resonance condition $\omega = \omega_D(\mathbf{r}, \mu, \beta_e)$ no longer selects a single geometric surface but broadens into a thin region centered around the drift-defined resonant surface, with thickness set by the velocity distribution.

To include the GR effects, we fix the compactness of the NS at

$$u \equiv \frac{2GM}{Rc^2} = 0.3, \tag{4-1}$$

and the other NS parameters are held consistent with the previous section. Since all photons experience nearly the same redshift from emission to scattering in our geometries, GR mainly introduces a common rescaling in the intensity and energy. Therefore, we interpret the surface temperature kT_s as the effective blackbody temperature of X-ray emission just before scattering, the same as in Section 3.

Under the current model, the scattering is controlled by the parameter set:

$$\{\xi_\tau, \beta_0, kT_e, kT_s, \theta, M\}. \tag{4-2}$$

In the survey below, we fix kT_s, $E_{\rm ad}$, and M, and vary $(\xi_\tau, \beta_0, kT_e, \theta)$, while all other parameters are the same as in Section 3.

Compared with the simplified model in the previous chapter, an important difference in the full model is that, after including the thermal velocity distribution of the plasma and relativistic effects, parameter variations no longer enter the results only by changing the density and hence the scattering strength. Instead, they also affect the scattering location, Doppler shift, efficiency of mode redistribution, and projection of the viewing geometry. Therefore, when interpreting the parameter study below, we focus mainly on two diagnostic quantities: first, the changes in the mode-resolved fluxes relative to the unscattered case, and second, the deviation of the linear polarization degree from the initial vacuum-resonance signal.

4.1 Optical-depth dependence

Before analyzing the spectra and polarization, it is useful to delineate under what conditions the single-scattering solution is valid. The resonant optical depth τ_α (for mode α) is primarily controlled by (ξ_τ, β_0), which set the electron density and beaming.

Figure 4-1 presents the heatmap of the characteristic optical depth τ_0 (see Eq. (2-38)), calculated at $kT_e = 10$ keV and $\theta = 35^\circ$, as functions of ξ_τ and β_0. The $\tau_0 = 1$ contour marks the single-scattering boundary; the $\tau_0 = 0.4$ contour corresponds to $\lesssim 10\%$ error for a first-order expansion of $\exp(-\tau)$. As expected, larger ξ_τ and smaller β_0 yield higher τ_α due to the increased particle density. Physically, this optical-depth map first delineates the regime of applicability for the results in this chapter: for parameter combinations with $\tau \lesssim 1$, the single-scattering approximation may be regarded as approximately valid; for parameter combinations with $\tau \lesssim 0.4$, the single-scattering solution is expected to be reasonably reliable.

In addition, the optical-depth map also provides a useful reference for interpreting the results in the subsequent parameter study: for instance, if a certain behavior is observed in the regime $\tau \lesssim 0.4$, it can be confidently attributed to single-scattering effects; if it is observed in the regime $\tau \gtrsim 1$, it should not be regarded as a strict quantitative prediction of single scattering.

We adopt $\tau_0 = 0.4$ as a relatively conservative reference line because the single-scattering solution in this work is essentially a low-optical-depth expansion of the attenuation term and the scattering source term. Taking the attenuation factor as an example,

$$\exp(-\tau) = 1 - \tau + \frac{\tau^2}{2} + \mathcal{O}(\tau^3), \tag{4-3}$$

the neglected second-order term is of order $\tau^2/2$. When $\tau = 0.4$, this term is approximately $0.08 < 10\%$, and can therefore serve as an empirical boundary below which the first-order results remain reasonably reliable. Once τ exceeds ~ 1, multiple scattering, mode energy redistribution, and photon escape probability all become important. In that regime, the results in this chapter can still be used to assess qualitative trends, but should not be interpreted as strict quantitative predictions.

Using the twist parametrization defined in Eq. (2-5), the total pole-to-pole twist

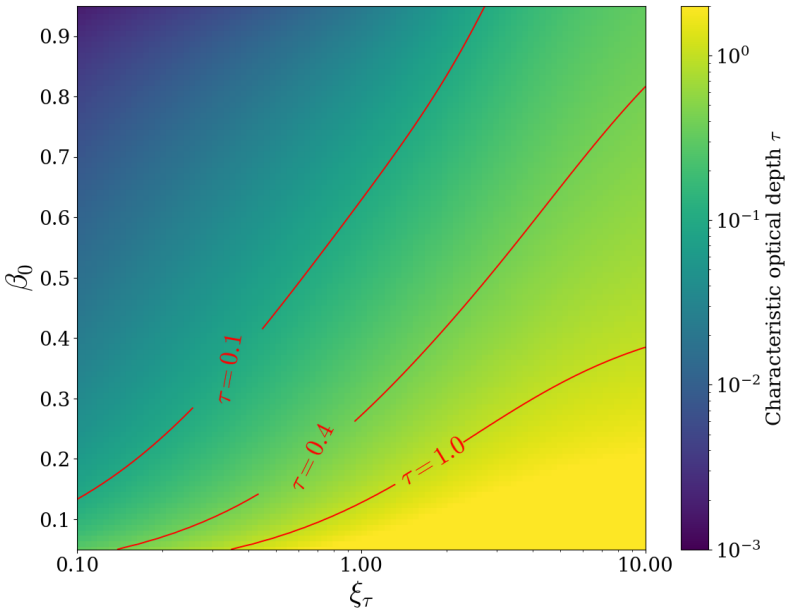

Figure 4-1 Heatmap of the characteristic resonant optical depth in the full model. The parameters are: $B_{\rm p} = 10^{14}$ G, $R = 10$ km, $kT_e = 10$ keV, $kT_s = 0.6$ keV, a hot spot at $(\theta_s, \phi_s) = (53^\circ, 37^\circ)$, and viewing angle $\theta = 35^\circ$. Contours for $\tau_\alpha = 1$ and $\tau_\alpha = 0.4$ delineate the validity regime of the single-scattering/first-order approximation.

angle is approximately

$$\Delta\phi = \int_0^\pi \frac{B_\phi}{B_\theta \sin\theta}\, \mathrm{d}\theta \sim \pi\xi_\tau, \tag{4-4}$$

so the ranges adopted in previous Monte Carlo studies (e.g., Nobili et al. 34, Fernández et al. 11) fall largely within the $\tau_0 \lesssim 1$ regime in Figure 4-1.

4.2 Spectra and polarization

We survey four key parameters: the viewing angle θ, the magnetic twist ξ_τ, the mean drift speed of electrons β_0, and the plasma temperature kT_e. The observed flux is computed as a multidimensional integral over the emission direction, scattering geometry, and electron velocity. Given the smoothness of the integration kernel, we evaluate the integral via Monte Carlo quadrature with 10^6 samples per configuration. This choice introduces small statistical fluctuations, or "noise", in the results, but enables significantly improved computational speed and numerical stability, resulting in a relative numerical uncertainty below 0.5%.

The following four sets of parameters do not control the results in mutually inde-

pendent ways, but instead highlight different physical effects: θ mainly changes the magnetic-field direction seen by the observer and the projection of the hot spot; ξ_τ mainly regulates the magnetospheric current and scattering optical depth; β_0 simultaneously controls the electron density and the relativistic Doppler effect; and kT_e sets the width of the electron velocity distribution. In other words, the parameter study in this section is not merely a numerical survey, but is designed to separate, one by one, the roles of geometric effects, density effects, bulk drift, and thermal broadening.

Viewing geometry. Figures 4-2 and 4-3 present the flux and polarization spectra for various viewing angles. For this plot, we consider a single hot spot located at the equator $(\theta_s, \phi_s) = (90^\circ, 37^\circ)$ to highlight the north–south asymmetries [see 34]. Notably, pairs of LOS angles symmetric about the equator (e.g., 37° and 143°) yield markedly different flux and polarization spectra, demonstrating the impact of Doppler shifts caused by large-scale net currents flowing from magnetic north to south. Importantly, the polarization curves retain the qualitative behavior previously seen in Section 3: RCS may suppress or erase the intrinsic mode-conversion feature that would otherwise appear in the emission. For instance, the curve corresponding to $\theta = 37^\circ$ shows sign flips in polarization degree, whereas for other angles $P_{\rm L}$ remains positive across the energy band. We verify that in this parameter setting, the optical depth $\tau_\alpha(\theta)$ remains well below unity (typically $\lesssim 0.15$), indicating that even single scattering events can significantly modify the polarization signature, despite the overall low scattering probability. This is not expected in the simplified-model study in Section 3.

This north–south asymmetry is one of the most important new features of the full model relative to the simplified model in Section 3. In the cold-plasma, non-relativistic approximation, symmetric lines of sight usually change only the projected area and path length. However, when the electrons have a mean drift velocity, the Doppler factor in the resonance condition breaks this simple symmetry. The relevant factor can be written as

$$\mathcal{D}(\beta_e, \mu) = \frac{1}{\gamma_e(1-\beta_e\mu)}, \qquad \omega_D = \mathcal{D}\,\omega_B, \tag{4-5}$$

where $\mu = \widehat{\Omega}\cdot\widehat{B}$. For a hot spot located near the magnetic equator, even if photons from the northern and southern directions have the same μ relative to the electron drift

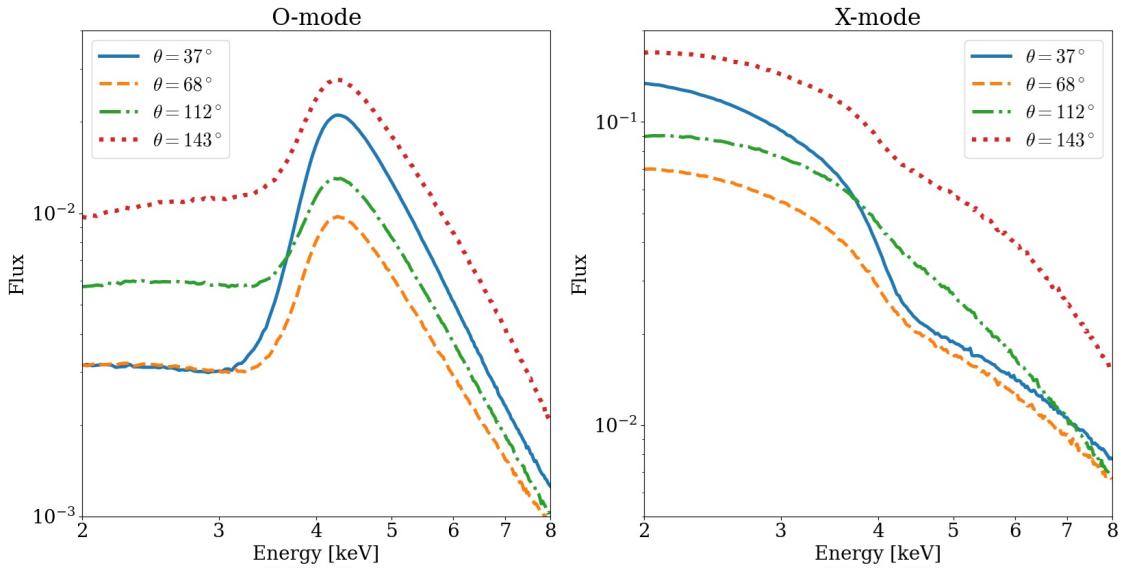

Figure 4-2 Flux spectra for different viewing angles in the full model. The parameters are: $B_{\rm p} = 10^{14}$ G**,** $R = 10$ km**,** $kT_e = 10$ keV**,** $kT_s = 0.6$ keV**,** $\xi_\tau = 0.2$**,** $\beta_0 = 0.5$**, and a hot spot at** $(\theta_s, \phi_s) = (90°, 37°)$**. Results are shown for the viewing angles** $\theta = 37°, 68°, 112°, 143°$**.**

direction, a nonzero directed electron drift velocity still changes the effective resonant radius, the scattering cross-section weights, and the rescaling of the radiation intensity. Therefore, the results for θ and $\pi - \theta$ are no longer equivalent. In other words, the viewing angle is not only a geometrical parameter, but also also a factor that participates in determining the dynamical efficiency of RCS through the Doppler factor.

Magnetic twist. Figures 4-4 and 4-5 explore how varying the magnetic twist ξ_τ affects the resulting flux and polarization spectra. The twist primarily modulates the plasma density and hence the scattering strength. As ξ_τ increases, the flux spectra show progressively larger deviations from the unscattered case, exhibiting the "spectral smoothing" noted in Section 3. However, relativistic effects become more prominent in the polarization spectra, especially at higher photon energies. Compared to the non-relativistic case, special-relativistic effects cause the polarization degree to rise again at higher energies. In some cases, the polarization curve crosses zero twice within the IXPE band, indicating the possibility of multiple 90° PA swings (this is also seen in a pure QED scenario; see Lai 26 and Kelly et al. 27). For sufficiently large ξ_τ, polarization remains strictly positive, and mode switching disappears.

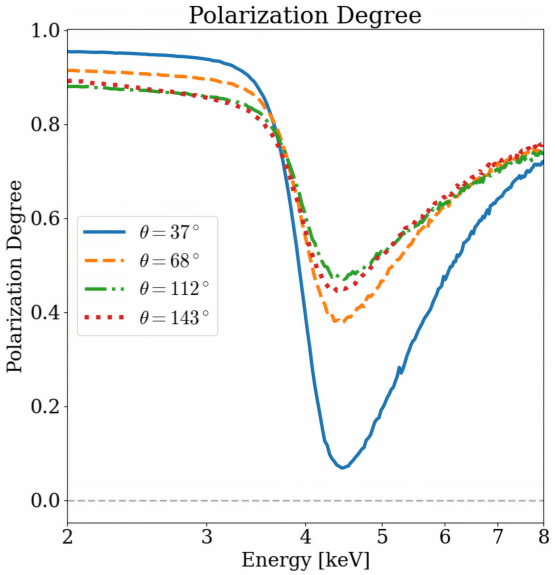

Figure 4-3 Polarization spectra for different viewing angles in the full model. The parameters are: $B_{\rm p} = 10^{14}$ G, $R = 10$ km, $kT_e = 10$ keV, $kT_s = 0.6$ keV, $\xi_\tau = 0.2$, $\beta_0 = 0.5$, **and a hot spot at** $(\theta_s, \phi_s) = (90^\circ, 37^\circ)$. **Results are shown for the viewing angles** $\theta = 37^\circ, 68^\circ, 112^\circ, 143^\circ$.

The results for the magnetic-twist parameter can be understood on two levels. First, increasing ξ_τ is equivalent to strengthening the magnetospheric current, thereby increasing the electron number density participating in RCS and enhancing the weight of the scattered-in term relative to the direct attenuation term. Second, the twisted magnetic field also changes the local magnetic-field direction, and therefore changes the angular distributions of $\widehat{\Omega}' \cdot \widehat{B}$ and $\widehat{\Omega} \cdot \widehat{B}$, as well as the scattering matrix elements between polarization modes. Thus, ξ_τ is not merely a parameter that regulates the optical depth; it also changes the scattering geometry.

To describe more clearly the dominant polarization-mode transition in the figures, the mode-switching energy can be defined by the zero point of $P_{\rm L}$:

$$P_{\rm L}(E_{\rm sw}) = 0, \qquad N_{\rm sw} \equiv \#\{E \in [2,8]\ \text{keV} : P_{\rm L}(E) = 0\}. \tag{4-6}$$

Here $N_{\rm sw}$ denotes the number of times that the polarization curve crosses zero within the IXPE band. The unscattered or weakly scattered cases usually correspond to one mode switch induced by vacuum resonance. At intermediate ξ_τ, however, RCS and relativistic effects may introduce an additional zero crossing. When ξ_τ increases further, the X-

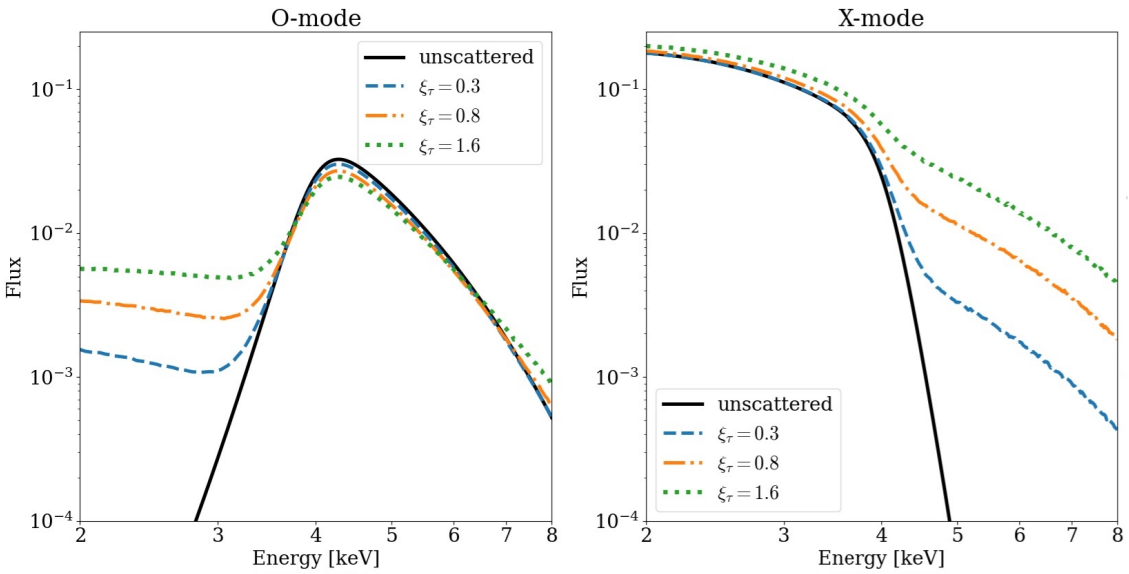

Figure 4-4 Flux spectra for different magnetospheric twist parameters in the full model. The parameters are: $B_{\rm p} = 10^{14}$ G, $R = 10$ km, $kT_e = 10$ keV, $kT_s = 0.6$ keV, $\theta = 35°$, $\beta_0 = 0.5$, and a hot spot at $(\theta_s, \phi_s) = (53°, 37°)$. Results are shown for magnetic twist $\xi_\tau = 0.3, 0.8, 1.6$, and are compared with the unscattered case.

mode is continuously replenished and $P_{\rm L}$ is lifted as a whole, causing all zero crossings to disappear instead. This behavior, in which an additional zero appears and then disappears, is one of the richer results exhibited by the full model relative to the simplified version.

Electron drift velocity. Figures 4-6 and 4-7 show the impact of changing the average drift velocity β_0 on the flux and polarization spectra. Like ξ_τ, the parameter β_0 influences both the plasma density and the strength of SR beaming. While its effects on the flux spectrum resemble those of increasing ξ_τ, the behavior of the polarization curves offers further diagnostic insight. Decreasing β_0 increases the particle density and weakens SR beaming, suppressing $P_{\rm L}$ at low energies and flattening its high-energy tail that was initially raised by SR; this is consistent with the non-relativistic trend discussed in Section 3. However, in terms of the first zero-crossing energy—the location where the initial 90° PA swing occurs—the effect of varying β_0 is subtler than that of ξ_τ. The transition slopes remain similar, indicating that β_0 mainly sets the vertical offset (baseline) of $P_{\rm L}$, while it plays a secondary role in determining the slope that shapes the crossing location. [2]

[2] A dynamic analogy may be helpful: imagine the polarization curve as a catenary suspended between a high left platform and a vertical wall on the right. Increasing relativistic effect raises the right anchor,

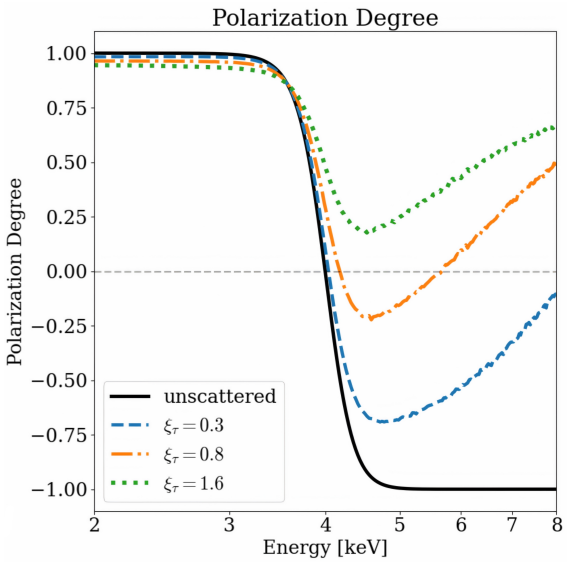

Figure 4-5 Polarization spectra for different magnetospheric twist parameters in the full model. The parameters are: $B_{\rm p} = 10^{14}$ G, $R = 10$ km, $kT_e = 10$ keV, $kT_s = 0.6$ keV, $\theta = 35°$, $\beta_0 = 0.5$, **and a hot spot at** $(\theta_s, \phi_s) = (53°, 37°)$. **Results are shown for magnetic twist** $\xi_\tau = 0.3, 0.8, 1.6$, **and are compared with the unscattered case.**

The physical role of β_0 is more complex than that of ξ_τ, because it enters both the electron number density and the relativistic transformations. On the one hand, $n_e \propto \beta_0^{-1}$ indicates that a smaller drift velocity corresponds to a higher charge density and a larger scattering probability. On the other hand, a larger β_0 strengthens Doppler beaming and makes the redistribution of scattered photons in energy and direction more prominent. Therefore, variations in β_0 do not always correspond one-to-one to stronger or weaker scattering. In the low-β_0 regime, the density effect dominates and mainly appears as an overall suppression of the polarization degree. In the high-β_0 regime, relativistic effects dominate and mainly appear as a rise of $P_{\rm L}$ at the high-energy end and a change in the slope of the curve. This also shows that the influence of β_0 on the polarization spectrum is more diagnostically useful than its influence on the total flux.

Together, these two main control parameters, ξ_τ and β_0, determine how RCS reshapes polarization spectra mainly through changing magnetospheric density and special-relativistic effects. Two principal effects emerge: (i) a reduction in both the absolute value and spectral variation of the polarization degree; and (ii) a high-energy rise of $P_{\rm L}$ driven

steepening the tail of the curve while leaving its middle largely unchanged.

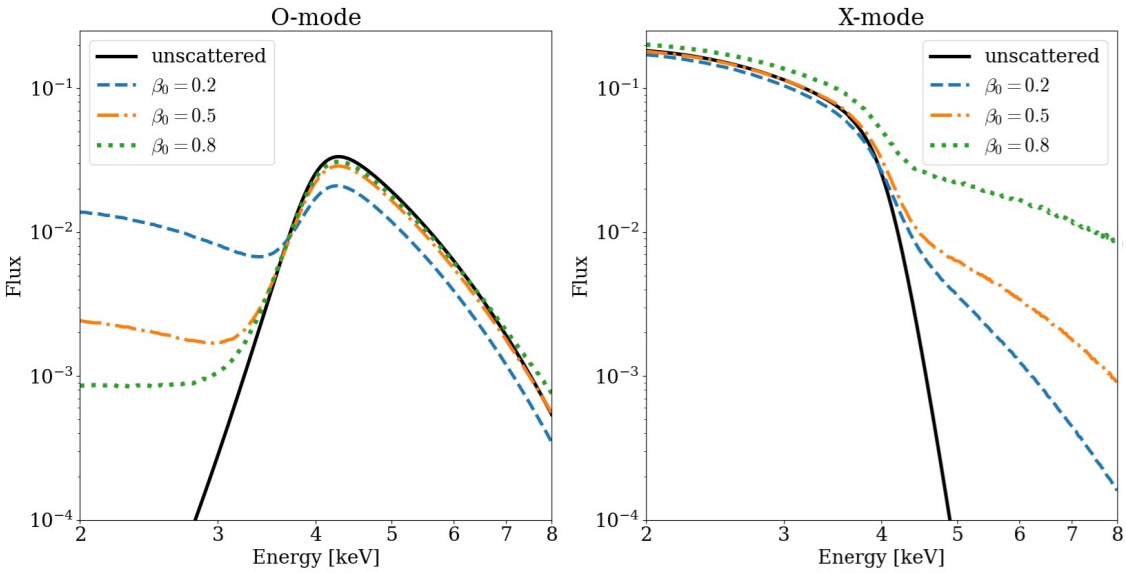

Figure 4-6 Flux spectra for different mean electron drift velocities in the full model. The parameters are: $B_{\rm p} = 10^{14}$ G, $R = 10$ km, $kT_e = 10$ keV, $kT_s = 0.6$ keV, $\theta = 35°$, $\xi_\tau = 0.5$, and a hot spot at $(\theta_s, \phi_s) = (53°, 37°)$. Results are shown for $\beta_0 = 0.2, 0.5, 0.8$, and are compared with the unscattered case.

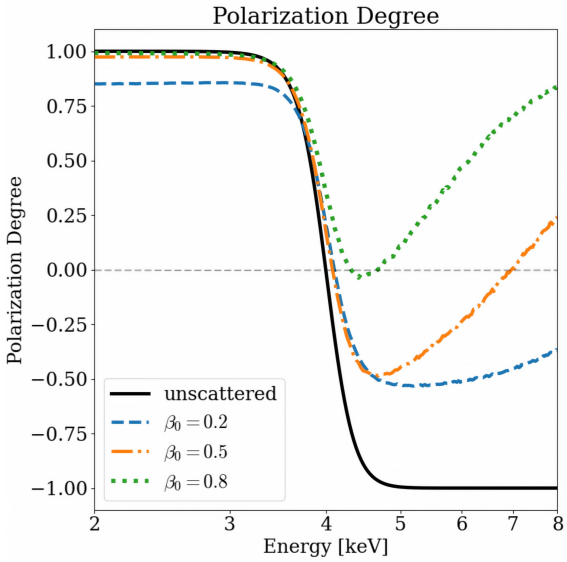

Figure 4-7 Polarization spectra for different mean electron drift velocities in the full model. The parameters are: $B_{\rm p} = 10^{14}$ G, $R = 10$ km, $kT_e = 10$ keV, $kT_s = 0.6$ keV, $\theta = 35°$, $\xi_\tau = 0.5$, and a hot spot at $(\theta_s, \phi_s) = (53°, 37°)$. Results are shown for $\beta_0 = 0.2, 0.5, 0.8$, and are compared with the unscattered case.

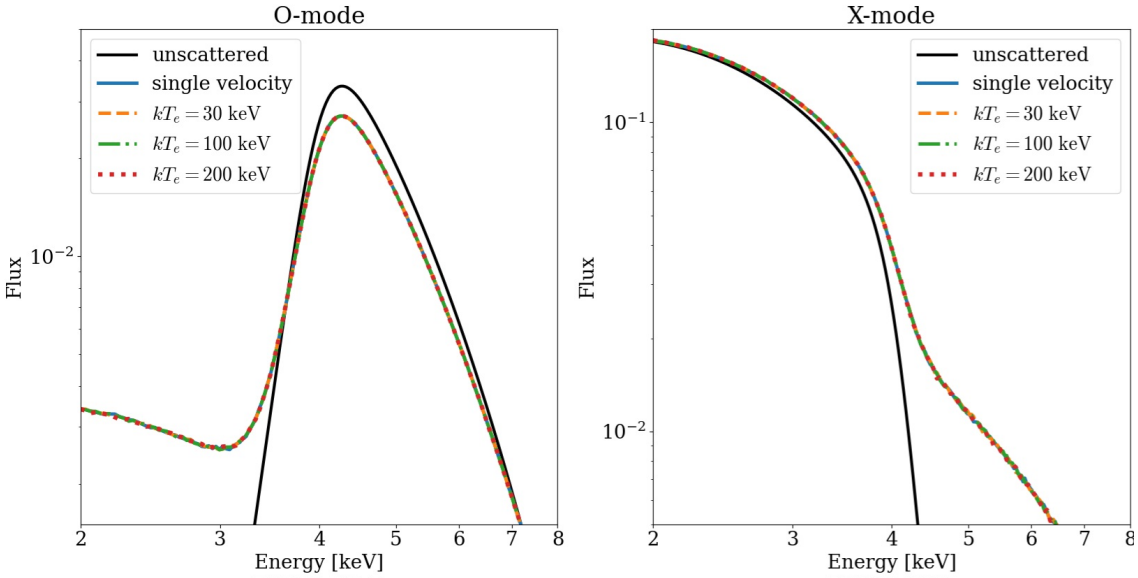

Figure 4-8 Flux spectra for different magnetospheric plasma temperatures in the full model. The parameters are: $B_{\rm p} = 10^{14}$ G, $R = 10$ km, $kT_s = 0.6$ keV, $\theta = 35°$, $\xi_\tau = 0.8$, $\beta_0 = 0.5$, and a hot spot at $(\theta_s, \phi_s) = (53°, 37°)$. Results are shown for $kT_e = 30, 100, 200$ keV, and are compared with the unscattered and single-velocity cases.

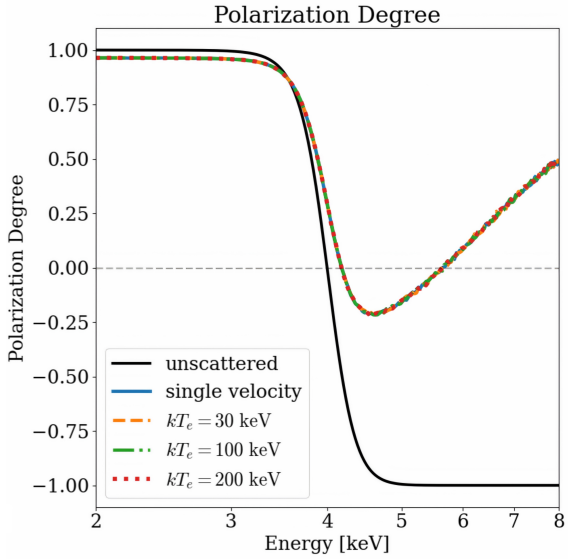

Figure 4-9 Polarization spectra for different magnetospheric plasma temperatures in the full model. The parameters are: $B_{\rm p} = 10^{14}$ G, $R = 10$ km, $kT_s = 0.6$ keV, $\theta = 35°$, $\xi_\tau = 0.8$, $\beta_0 = 0.5$, and a hot spot at $(\theta_s, \phi_s) = (53°, 37°)$. Results are shown for $kT_e = 30, 100, 200$ keV, and are compared with the unscattered and single-velocity cases.

by SR mode redistribution. Even in the single-scattering regime, RCS may erase the mode-switch feature that is originally present in the emission. To understand this trend, consider the polarized RCS cross sections in the ERF (see Eq. (2-31)):

$$\begin{aligned}\sigma_{1-1} &= \frac{1}{3}\sigma_{1-2} = \frac{\pi^2 e^2}{2m_e c}\delta(\omega-\omega_B)\left(\Omega'\cdot\widehat{\mathbf{B}}\right)^2,\\ \sigma_{2-2} &= 3\sigma_{2-1} = \frac{3\pi^2 e^2}{2m_e c}\delta(\omega-\omega_B).\end{aligned} \tag{4-7}$$

These expressions represent the relative probabilities for photons to scatter between specific initial and final polarization states. Notably, regardless of the initial state, scattering tends to populate the X-mode (the polarization index $\alpha = 2$) more efficiently. Since the original emission is X-dominated at low energies, RCS has a limited effect there, whereas at higher energies (O-dominated) RCS transfers power to the X-mode, producing the characteristic high-energy rise of $P_{\rm L}$. The electron density mainly rescales $P_{\rm L}$, while the SR effects modulate its slope, particularly in the high-energy tail. Together, they reshape the polarization distribution and influence the energy at which mode switches occur.

This point also explains why variations in the total flux are sometimes less pronounced than those in the polarization degree. The total flux depends on the sum of the two modes, $\mathcal{I}^1 + \mathcal{I}^2$, whereas the polarization degree depends on their difference, $\mathcal{I}^2 - \mathcal{I}^1$. If RCS mainly redistributes photons between the two polarization modes without substantially changing the total photon number, then the total flux spectrum may show no significant change, while $P_{\rm L}$ can still vary appreciably. Observationally, this means that even if RCS has only a weak effect on the total spectrum in the 2–8 keV band, it may still leave a clear signature through the energy-dependent variation of the linear polarization degree, the presence or absence of a 90° polarization-angle swing, and the slope of the high-energy polarization degree.

Thermal broadening. Finally, Figures 4-8 and 4-9 examine the role of plasma temperature kT_e in shaping the flux and polarization spectra. For visibility, the flux panels are vertically rescaled. Compared to the single-velocity case, thermal motion induces only modest changes. Unlike β_0, which parameterizes the bulk drift, increasing kT_e only broadens the velocity distribution around β_0. This tends to average out the variation in

Doppler effects over electron speeds, resulting in behavior that closely resembles the single-velocity case at the same β_0. This is consistent with previous findings by Nobili et al. [34].

From the computational expression, the role of temperature is mainly reflected in averaging the scattering kernel over different electron velocities:

$$\langle K_{\alpha\beta}\rangle_{T_e} = \int_{-1}^{1} f_1(\beta_e;\beta_0,T_e)\, K_{\alpha\beta}(\beta_e)\,\mathrm{d}\beta_e. \tag{4-8}$$

As kT_e increases, f_1 broadens, and the Doppler factors and resonant locations corresponding to different β_e are averaged over, so sharp velocity-dependent structures are smoothed out. However, as long as the velocity distribution remains centered around the same bulk drift velocity β_0, the averaged result usually does not deviate significantly from the single-velocity case. This indicates that, within the present parameter range, the first-order factor controlling the shape of the polarization spectrum is the mean drift velocity rather than the thermal velocity dispersion; temperature acts more as a higher-order smoothing effect.

Power-law-like component and the production of non-thermal spectra. According to Nobili et al. [34, 44] and subsequent full Monte Carlo radiative-transfer studies of the total X-ray radiation spectrum, when magnetar soft X-ray emission is fitted with the empirical "blackbody + power-law" ("BB+PL") spectral model, seed blackbody radiation can produce an approximately power-law non-thermal spectral component through multiple RCS. It should be noted that the single-scattering semi-analytical model in this work can partially demonstrate the hardening effect of RCS on the seed blackbody spectrum, and can produce a relatively significant approximately power-law component in a global effective spectral fit. The scattered spectrum also forms a hard-photon excess at high energies, but it cannot produce a genuine power-law continuum across the entire X-ray band.

Following the empirical XSPEC fitting procedure [60, 61], the global "BB+PL" spectral fit to magnetar radiation can be written as

$$n(E) \equiv \frac{\mathcal{F}_\omega^1 + \mathcal{F}_\omega^2}{E} = n_{\mathrm{BB}}(E) + n_{\mathrm{PL}}(E) = A_{\mathrm{BB}}\frac{E^2}{\exp(E/kT)-1} + A_{\mathrm{PL}}E^{-\Gamma_{\mathrm{eff}}}, \tag{4-9}$$

where $\mathcal{N}(E) \equiv \mathrm{d}N(E)/\mathrm{d}E$ denotes the photon number spectral density at the corresponding energy, and Γ_{eff} is the global effective photon index fitted over the entire IXPE band. For spectra with a local approximately power-law hard-photon excess, this index is usually in the range 2–4. After obtaining the two globally fitted spectral components, the fraction of either the blackbody or the power-law component in the total observed spectrum can be defined as

$$w_i(E) = \mathcal{N}_i(E)/(\mathcal{N}_{\mathrm{BB}}(E) + \mathcal{N}_{\mathrm{PL}}(E)), \tag{4-10}$$

To assess the reliability of the power-law spectral component, one can use the globally fitted $\mathcal{N}_{\mathrm{BB,PL}}$ to study the behavior of the photon index of the power-law component across the IXPE band. The photon index of the locally fitted spectrum can be written as

$$\Gamma_{\mathrm{tot}}(E) = -\frac{d\ln[\mathcal{N}_{\mathrm{BB}}(E) + \mathcal{N}_{\mathrm{PL}}(E)]}{d\ln E} = w_{\mathrm{BB}}(E)\Gamma_{\mathrm{BB}}(E) + w_{\mathrm{PL}}(E)\Gamma_{\mathrm{PL}}(E), \tag{4-11}$$

where the local photon index contributed by the blackbody spectrum is

$$\Gamma_{\mathrm{BB}}(E) = -2 + \frac{E/kT}{1 - \exp(-E/kT)}. \tag{4-12}$$

After substituting the above expression and solving for Γ_{PL}, one can examine its behavior over the entire IXPE band and determine whether it corresponds to a genuine approximately power-law distribution. If the resulting Γ_{PL} lies in the range 2–4 and remains approximately constant, then the semi-analytical model in this work can be regarded as predicting that seed blackbody radiation produces an approximately power-law spectral component through RCS.

Figure 4-10 shows a typical flux-fitting result calculated from the semi-analytical model. The final spectrum can be fitted well by a global photon index corresponding to $\Gamma_{\mathrm{eff}} \simeq 3.0$, consistent with the empirical range $\Gamma \sim$ 2–4. At the same time, the fraction of the PL component increases from 0.2 at low energies to 0.8 at high energies, indicating that RCS can indeed produce an approximately power-law spectral shape in the soft X-ray radiation spectrum and allow this component to become increasingly dominant at high energies, reflecting the partial hardening of the thermal photon spectrum through

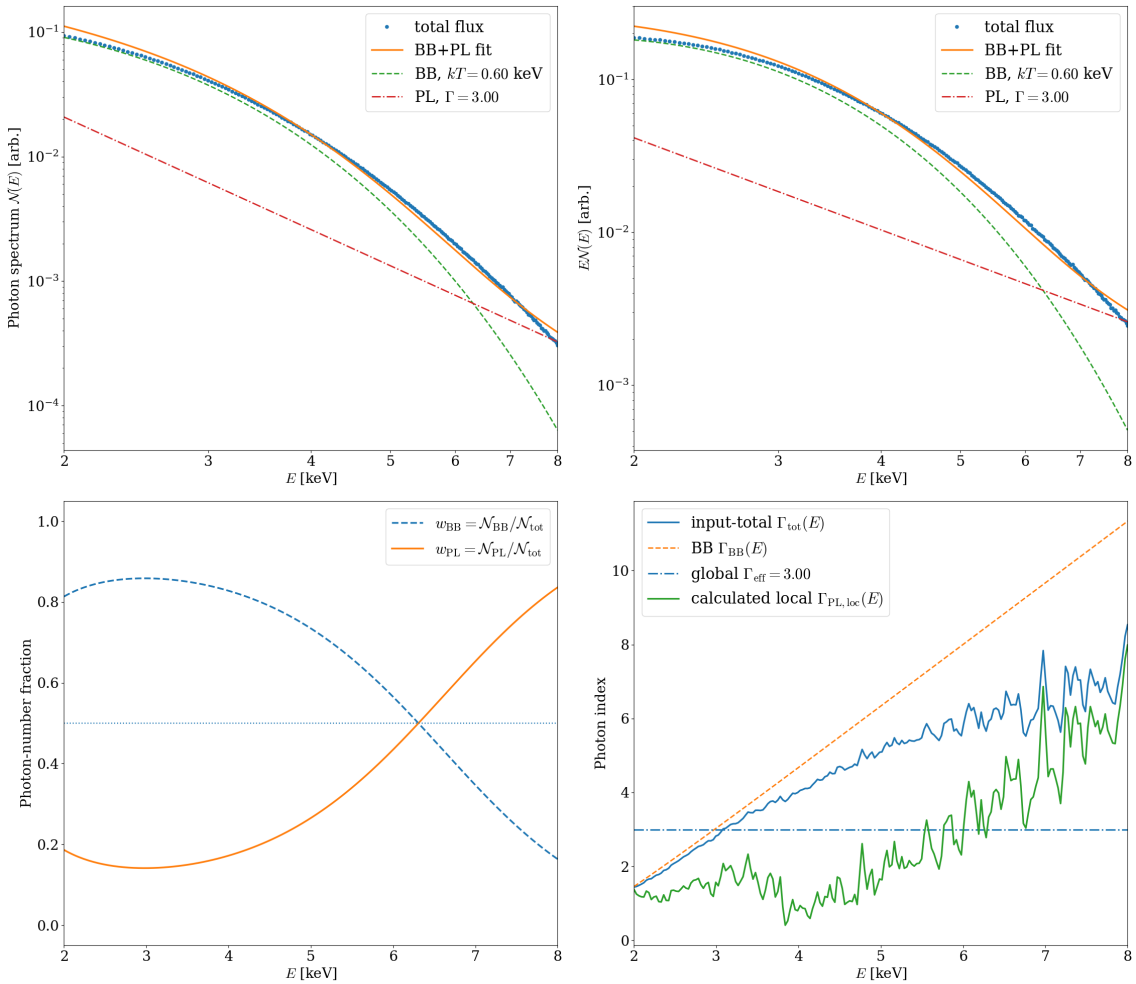

Figure 4-10 Total spectrum fit and photon index for the calculated typical total observed flux in the full model. The parameters are: $B_{\rm p} = 10^{14}$ G, $R = 10$ km, $kT_s = 0.6$ keV, $\theta = 35^\circ$, $\xi_\tau = 0.8$, $\beta_0 = 0.5$, and a hot spot at $(\theta_s, \phi_s) = (53^\circ, 37^\circ)$. The upper panels show the fitting result for photon number and energy flux with "BB+PL" spectra. The lower left panel shows the fractions of the BB-like and PL-like components in the observed flux as functions of energy. The lower right panel shows the local energy-dependent photon index from Eqs. (4-11) and (4-12) as a function of energy (green line), compared with the global fixed effective photon index (blue dashed line), indicating the strong energy dependence of the local photon index fitted from the observed flux.

Doppler shifts. However, the overall fitting result is still insufficient to directly conclude that RCS efficiently produces a PL tail. As shown in the lower-right panel of Figure 4-10, for a true power-law component, the locally fitted $\Gamma_{\rm PL}$ should remain approximately constant across the IXPE band. In contrast, the figure shows that $\Gamma_{\rm loc}$ fluctuates significantly relative to $\Gamma_{\rm eff}$, indicating that the residual component obtained after subtracting the blackbody radiation from the total spectrum can only qualitatively display part of the approximately power-law behavior after Comptonization. Although the high-energy PL component gradually becomes dominant, the overly large and strongly varying local photon index is still insufficient to robustly support the conclusion that the single-scattering semi-analytical RCS model in this work can produce a power-law tail.

4.3 Main conclusion

The parameter study of the full model in this chapter shows that the soft X-ray polarization spectra of magnetars are highly sensitive to the physical parameters of the magnetosphere. Compared with the simplified model in the previous chapter, relativistic effects in the full model allow even single RCS events at low optical depth, with $\tau \ll 1$, to significantly change the shape of $P_{\rm L}(E)$. This indicates that erasing or reshaping the mode-switching feature induced by QED vacuum resonance does not necessarily require high-optical-depth multiple scattering; a low-optical-depth magnetosphere with significant bulk drift can also produce observable effects.

Specifically, the viewing angle θ controls the geometric projection and Doppler-induced north–south asymmetry, and is the main factor determining the differences among polarization spectra for different lines of sight. The magnetic twist ξ_τ mainly strengthens RCS by increasing the current density, but it also changes the local magnetic-field geometry. The mean drift velocity β_0 simultaneously reduces the charge density and enhances the relativistic Doppler effect, and is therefore especially important for the high-energy slope of the polarization curve. The electron temperature kT_e mainly leads to velocity-distribution averaging and has a relatively weak influence on the polarization spectra within the present parameter range. Overall, ξ_τ and β_0 are the two most important magnetospheric parameters: the former mainly controls the scattering strength, while the latter mainly controls relativistic redistribution. According to the XSPEC fitting

results for a typical spectrum, the full single-scattering semi-analytical RCS model in this work can partially match the empirical "blackbody plus power-law" spectral form and yield a global effective photon index $\Gamma_{\rm eff}$ consistent with empirical values. However, by fitting the energy-dependent local photon index and examining its behavior, one still cannot conclude that this model robustly produces an ideal approximately power-law high-energy tail.

From an observational perspective, the most important result of this chapter is that RCS can suppress the energy dependence of the polarization degree, change the energy location of the 90° polarization-angle swing, and even cause the mode switch originally produced by vacuum resonance to disappear or generate additional mode switches. Therefore, if future observations detect an energy-dependent rotation of the magnetar polarization angle, it should not be attributed directly and simply to pure atmospheric QED vacuum resonance. Conversely, if no clear rotation is observed, the vacuum-resonance effect should not be ruled out immediately, because significant magnetospheric RCS may already have modified the original signal.

4.4 Research outlook

The results in this chapter are still based on several simplifying assumptions. First, we adopt a single hot spot as the radiation source, which helps isolate geometric effects, but the surface of a real magnetar may contain multiple hot regions or emit approximately over the whole surface. Phase superposition from multiple emitting regions can average out part of the geometric differences and may also change the zero-crossing structure of $P_{\rm L}$. Second, we still adopt an idealized treatment of the surface radiation induced by vacuum resonance in the magnetar atmosphere, whereas a more complete physical model requires a detailed description of the atmospheric radiation spectrum. Finally, we use a first-order single-scattering approximation, which is therefore suitable for describing the low-optical-depth regime. For strongly twisted magnetospheres with $\tau \gtrsim 1$, multiple scattering and energy redistribution must be included to obtain more reliable energy and polarization spectra.

Future work can proceed in four directions. First, the present single-hot-spot model can be extended to whole-surface or multi-temperature-zone emission models, allowing

phase-resolved polarization that varies with the rotational phase to be calculated. Second, a complete atmospheric model including QED effects can be used to describe magnetar surface atmospheric radiation. Third, iterative or Monte Carlo methods can be used to treat high-optical-depth RCS and to test whether the low-optical-depth trends found in this chapter extend into the strong-scattering regime. Fourth, the model results can be combined with existing IXPE observations and simulated observations from future missions such as eXTP to jointly constrain ξ_τ, β_0, kT_e, and the hot-spot geometry. Through these extensions, the semi-analytical physical picture developed in this work can be further transformed into a magnetar polarization model that can be used directly for data interpretation.

5 Summary and Further Discussion

In this work, we have developed a unified and analytically tractable framework to approximate how resonant Compton scattering in the magnetosphere and QED vacuum resonance in the atmosphere jointly shape the X-ray spectra and polarization observed from magnetars. Starting from the polarized radiative transfer equation (2-46) with scattering, we adopt a first-order approximation in optical depth (see Eqs. (2-47), (2-48), and (2-51)), which effectively captures single scattering events, to compute the observed polarization fluxes (Eqs. (2-56)–(2-58)). For a concrete baseline, we adopt an idealized initial surface emission polarization pattern that mimics vacuum-resonant conversion—100% X-mode below 4 keV and 100% O-mode above, with a smooth transition in between (see [26])—and then quantify how RCS in the magnetosphere reshapes the observable polarization signatures. Our key findings are as follows:

1. Increasing the plasma density in the magnetosphere leads to an overall suppression of both the absolute value and spectral variation of polarization degree $P_{\rm L}$. In other words, RCS acts to compress the polarization curve toward a horizontal line located *above* zero, diminishing the polarization contrast (see Figs. 3-2 and 4-5).

2. Increasing the average electron drift velocity enhances the SR effects, which tend to raise $P_{\rm L}$ in the high-energy tail and steepen its slope. In some cases, an extra mode switch (i.e., sign change in $P_{\rm L}$, implying a 90° PA swing) induced by RCS may occur (see Figure 4-7).

3. The energy of the *first* mode switch is only weakly shifted by RCS in the parameter ranges explored here; the zero-crossing location remains largely tied to the stellar surface physics set by vacuum resonance.

4. In the strong RCS regime, the combined effects of increased plasma density and enhanced SR effects may entirely erase the signature of mode switch within the observed bandpass (2–8 keV), even when the QED-induced conversion is present in the initial emission. This is consistent with the mode-redistribution trend expected from the resonant cross sections (see Eq. (4-7)).

However, these conclusions should be interpreted in light of several simplifying assumptions:

(i) Our magnetospheric configuration is *prescribed* rather than dynamically self-consistent. As discussed in Section 2, the field and current systems are parameterized and do not enforce full force-free equilibrium. The actual magnetosphere is likely to be partly twisted rather than globally twisted, and the prescribed thermal velocity distribution in the magnetosphere may not capture some intrinsic physical effects [e.g., 33, who considered a power-law distribution of relativistic momentum]. In addition, the electron density prescription applied in this work might underestimate the RCS optical depth of the magnetosphere. According to studies of electron–positron pair density in the magnetosphere through kinetic modeling, the pair multiplicities can be moderately high [40–43], i.e., the total density $n_{e^+} + n_{e^-} \gtrsim 30 n_e$. If such high $e^{\pm}$ multiplicities apply in real magnetars, the single-scattering approximation may also be questionable in the full model setup.

(ii) Our sample results consider emission from a single surface patch. Radiation from the whole NS surface can be easily included in our formalism and will likely average out some geometric contrasts.

(iii) Our transport solution is only of first order in optical depth. Fully capturing the energy-dependent behavior (e.g., the power-law high-energy tail and Comptonization) and energy/polarization redistribution at high RCS optical depth requires higher-order solutions via iterative scattering treatments [e.g., for 1D iterative scattering, see 32].

(iv) Our adopted surface polarization pattern is idealized; a more realistic treatment would require detailed modeling of the NS surface and atmosphere.

Despite these limitations, the semi-analytic nature of our method offers a major computational advantage and physical transparency. It allows us to extract the main physical trends without the computational cost or complexity of full Monte Carlo simulations and reveals intuitive connections between model inputs and observable outcomes.

Looking ahead, two immediate extensions are natural. First, to better capture viewing-angle-dependent effects, full-surface integration should be implemented, which would remove projection biases from small-area sources and allow more realistic modeling of observation profiles. In our formalism, this only requires treating the coordinates

of the surface emission point as integration variables over solid angle. Second, including stellar rotation would allow phase-resolved predictions when the magnetic and spin axes are misaligned. In our framework, this is equivalent to a rotation of the LOS direction vector and tracking how the polarization signal evolves with phase, enabling the calculation of phase-resolved light curves and phase-averaged polarization profiles. These developments, together with higher-order scattering, will help connect magnetar surface and magnetosphere models with observations. Upcoming X-ray polarization missions, such as eXTP [62, 63], will have greatly enhanced polarization sensitivity and an extended energy band, providing simultaneous spectral, timing, and polarization data, thereby enriching the magnetar polarization sample for further studies.

References

[1] Shapiro S L, Teukolsky S A. Black holes, white dwarfs and neutron stars. The physics of compact objects[M/OL]. 1983. DOI: 10.1002/9783527617661.

[2] Gold T. Rotating Neutron Stars as the Origin of the Pulsating Radio Sources[J/OL]. Nature, 1968, 218(5143): 731-732. DOI: 10.1038/218731a0.

[3] Goldreich P, Julian W H. Pulsar Electrodynamics[J/OL]. Astrophys. J., 1969, 157: 869. DOI: 10.1086/150119.

[4] Woltjer L. X-Rays and Type I Supernova Remnants.[J/OL]. Astrophys. J., 1964, 140: 1309-1313. DOI: 10.1086/148028.

[5] Thompson C, Duncan R C. Neutron Star Dynamos and the Origins of Pulsar Magnetism [J/OL]. Astrophys. J., 1993, 408: 194. DOI: 10.1086/172580.

[6] Duncan R C, Thompson C. Formation of Very Strongly Magnetized Neutron Stars: Implications for Gamma-Ray Bursts[J/OL]. Astrophys. J. Lett., 1992, 392: L9. DOI: 10.1086/186413.

[7] Thompson C, Duncan R C. The soft gamma repeaters as very strongly magnetized neutron stars - I. Radiative mechanism for outbursts[J/OL]. Mon. Not. Roy. Astron. Soc., 1995, 275 (2): 255-300. DOI: 10.1093/mnras/275.2.255.

[8] Kouveliotou C, Dieters S, Strohmayer T, et al. An X-ray pulsar with a superstrong magnetic field in the soft γ-ray repeater SGR1806 - 20[J/OL]. Nature, 1998, 393(6682): 235-237. DOI: 10.1038/30410.

[9] Kaspi V M, Beloborodov A M. Magnetars[J/OL]. Annu. Rev. Astron. Astrophys., 2017, 55 (1): 261-301. DOI: 10.1146/annurev-astro-081915-023329.

[10] Woods P M, Thompson C. Soft gamma repeaters and anomalous X-ray pulsars: magnetar candidates[M/OL]//Lewin W H G, van der Klis M. Compact stellar X-ray sources: Vol. 39. 2006: 547-586. DOI: 10.48550/arXiv.astro-ph/0406133.

[11] Fernández R, Davis S W. The X-ray Polarization Signature of Quiescent Magnetars: Effect of Magnetospheric Scattering and Vacuum Polarization[J/OL]. Astrophys. J., 2011, 730(2): 131. DOI: 10.1088/0004-637X/730/2/131.

[12] Weisskopf M C, Soffitta P, Baldini L, et al. The Imaging X-Ray Polarimetry Explorer (IXPE): Pre-Launch[J/OL]. Journal of Astronomical Telescopes, Instruments, and Systems, 2022, 8 (2): 026002. DOI: 10.1117/1.JATIS.8.2.026002.

[13] Taverna R, Turolla R. X-ray Polarization from Magnetar Sources[J/OL]. Galaxies, 2024, 12 (1): 6. DOI: 10.3390/galaxies12010006.

[14] Thompson C, Lyutikov M, Kulkarni S R. Electrodynamics of Magnetars: Implications for the Persistent X-Ray Emission and Spin-down of the Soft Gamma Repeaters and Anomalous X-Ray Pulsars[J/OL]. Astrophys. J., 2002, 574(1): 332-355. DOI: 10.1086/340586.

[15] Schwinger J. On Gauge Invariance and Vacuum Polarization[J/OL]. Physical Review, 1951, 82(5): 664-679. DOI: 10.1103/PhysRev.82.664.

[16] HEINZL T, LIESFELD B, AMTHOR K U, et al. On the observation of vacuum birefringence [J/OL]. Opt. Commun., 2006, 267: 318-321. DOI: 10.1016/j.optcom.2006.06.053.

[17] DI PIAZZA A, MULLER C, HATSAGORTSYAN K Z, et al. Extremely high-intensity laser interactions with fundamental quantum systems[J/OL]. Rev. Mod. Phys., 2012, 84: 1177. DOI: 10.1103/RevModPhys.84.1177.

[18] van Adelsberg M, Lai D. Atmosphere Models of Magnetized Neutron Stars: QED Effects, Radiation Spectra, and Polarization Signals[J/OL]. Mon. Not. Roy. Astron. Soc., 2006, 373: 1495-1522. DOI: 10.1111/j.1365-2966.2006.11098.x.

[19] Turolla R, Zane S, Watts A L. Magnetars: the physics behind observations. A review[J/OL]. Reports on Progress in Physics, 2015, 78(11): 116901. DOI: 10.1088/0034-4885/78/11/116901.

[20] Weisskopf M C, Ramsey B, O'Dell S, et al. The Imaging X-ray Polarimetry Explorer (IXPE) [C/OL]//den Herder J W A, Takahashi T, Bautz M. Society of Photo-Optical Instrumentation Engineers (SPIE) Conference Series: Vol. 9905 Space Telescopes and Instrumentation 2016: Ultraviolet to Gamma Ray. 2016: 990517. DOI: 10.1117/12.2235240.

[21] Taverna R, Turolla R, Muleri F, et al. Polarized x-rays from a magnetar[J/OL]. Science, 2022, 378(6620): 646-650. DOI: 10.1126/science.add0080.

[22] Zane S, et al. A Strong X-Ray Polarization Signal from the Magnetar 1RXS J170849.0-400910[J/OL]. Astrophys. J. Lett., 2023, 944(2): L27. DOI: 10.3847/2041-8213/acb703.

[23] Taverna R, Muleri F, Turolla R, et al. Probing magnetar magnetosphere through X-ray polarization measurements[J/OL]. Mon. Not. Roy. Astron. Soc., 2014, 438(2): 1686-1697. DOI: 10.1093/mnras/stt2310.

[24] Lai D, Ho W C. Resonant Conversion of Photon Modes Due to Vacuum Polarization in a Magnetized Plasma: Implications for X-Ray Emission from Magnetars[J/OL]. Astrophys. J., 2002, 566(1): 373-377. DOI: 10.1086/338074.

[25] Lai D, Ho W C. Polarized X-Ray Emission from Magnetized Neutron Stars: Signature of Strong-Field Vacuum Polarization[J/OL]. Phys. Rev. Lett., 2003, 91(7): 071101. DOI: 10.1103/PhysRevLett.91.071101.

[26] Lai D. IXPE detection of polarized X-rays from magnetars and photon mode conversion at QED vacuum resonance[J/OL]. Proceedings of the National Academy of Science, 2023, 120 (17): e2216534120. DOI: 10.1073/pnas.2216534120.

[27] Kelly R M E, Zane S, Turolla R, et al. X-ray polarization in magnetar atmospheres – effects of mode conversion[J/OL]. Mon. Not. Roy. Astron. Soc., 2024, 528(3): 3927-3940. DOI: 10.1093/mnras/stae159.

[28] Medin Z, Lai D. Density-functional-theory calculations of matter in strong magnetic fields. I. Atoms and molecules[J/OL]. Phys. Rev. A, 2006, 74(6): 062507. DOI: 10.1103/PhysRevA.74.062507.

[29] Medin Z, Lai D. Density-functional-theory calculations of matter in strong magnetic fields. II. Infinite chains and condensed matter[J/OL]. Phys. Rev. A, 2006, 74(6): 062508. DOI: 10.1103/PhysRevA.74.062508.

[30] Medin Z, Lai D. Condensed surfaces of magnetic neutron stars, thermal surface emission, and particle acceleration above pulsar polar caps[J/OL]. Mon. Not. Roy. Astron. Soc., 2007, 382(4): 1833-1852. DOI: 10.1111/j.1365-2966.2007.12492.x.

[31] Potekhin A Y, Chabrier G. Equation of state for magnetized Coulomb plasmas[J/OL]. Astron. Astrophys., 2013, 550: A43. DOI: 10.1051/0004-6361/201220082.

[32] Lyutikov M, Gavriil F P. Resonant cyclotron scattering and Comptonization in neutron star magnetospheres[J/OL]. Mon. Not. Roy. Astron. Soc., 2006, 368(2): 690-706. DOI: 10.1111/j.1365-2966.2006.10140.x.

[33] Fernández R, Thompson C. Resonant Cyclotron Scattering in Three Dimensions and the Quiescent Nonthermal X-ray Emission of Magnetars[J/OL]. Astrophys. J., 2007, 660(1): 615-640. DOI: 10.1086/511810.

[34] Nobili L, Turolla R, Zane S. X-ray spectra from magnetar candidates - I. Monte Carlo simulations in the non-relativistic regime[J/OL]. Mon. Not. Roy. Astron. Soc., 2008, 386(3): 1527-1542. DOI: 10.1111/j.1365-2966.2008.13125.x.

[35] Rea N, Zane S, Turolla R, et al. Resonant Cyclotron Scattering in Magnetars' Emission [J/OL]. Astrophys. J., 2008, 686(2): 1245-1260. DOI: 10.1086/591264.

[36] Zane S, Rea N, Turolla R, et al. X-ray spectra from magnetar candidates - III. Fitting SGR/AXP soft X-ray emission with non-relativistic Monte Carlo models[J/OL]. Mon. Not. Roy. Astron. Soc., 2009, 398(3): 1403-1413. DOI: 10.1111/j.1365-2966.2009.15190.x.

[37] Taverna R, Turolla R, Suleimanov V, et al. X-ray spectra and polarization from magnetar candidates[J/OL]. Mon. Not. Roy. Astron. Soc., 2020, 492(4): 5057-5074. DOI: 10.1093/mnras/staa204.

[38] Lai D, Ho W C. Transfer of Polarized Radiation in Strongly Magnetized Plasmas and Thermal Emission from Magnetars: Effect of Vacuum Polarization[J/OL]. Astrophys. J., 2003, 588(2): 962-974. DOI: 10.1086/374334.

[39] Heyl J S, Shaviv N J. QED and the high polarization of the thermal radiation from neutron stars[J/OL]. Phys. Rev. D, 2002, 66(2): 023002. DOI: 10.1103/PhysRevD.66.023002.

[40] Thompson C. Electrodynamics of Magnetars. IV. Self-Consistent Model of the Inner Accelerator with Implications for Pulsed Radio Emission[J/OL]. Astrophys. J., 2008, 688(1): 499-526. DOI: 10.1086/592061.

[41] Beloborodov A M. Electron-Positron Flows around Magnetars[J/OL]. Astrophys. J., 2013, 777(2): 114. DOI: 10.1088/0004-637X/777/2/114.

[42] Thompson C, Kostenko A. Pair Plasma in Super-QED Magnetic Fields and the Hard X-Ray/Optical Emission of Magnetars[J/OL]. Astrophys. J., 2020, 904(2): 184. DOI: 10.3847/1538-4357/abbe87.

[43] Zhang J, Thompson C. Quantum Plasma Creation near a Magnetar[J/OL]. Astrophys. J., 2025, 986(2): 173. DOI: 10.3847/1538-4357/adabde.

[44] Nobili L, Turolla R, Zane S. X-ray spectra from magnetar candidates - II. Resonant cross-sections for electron-photon scattering in the relativistic regime[J/OL]. Mon. Not. Roy. Astron. Soc., 2008, 389(2): 989-1000. DOI: 10.1111/j.1365-2966.2008.13627.x.

[45] Adler S L. Photon splitting and photon dispersion in a strong magnetic field.[J/OL]. Annals of Physics, 1971, 67: 599-647. DOI: 10.1016/0003-4916(71)90154-0.

[46] Heyl J S, Hernquist L. Birefringence and dichroism of the QED vacuum[J/OL]. J. Phys. A, 1997, 30: 6485-6492. DOI: 10.1088/0305-4470/30/18/022.

[47] Heisenberg W, Euler H. Folgerungen aus der Diracschen Theorie des Positrons[J/OL]. Zeitschrift fur Physik, 1936, 98(11-12): 714-732. DOI: 10.1007/BF01343663.

[48] Heyl J S, Hernquist L. Analytic form for the effective Lagrangian of QED and its application to pair production and photon splitting[J/OL]. Phys. Rev. D, 1997, 55(4): 2449-2454. DOI: 10.1103/PhysRevD.55.2449.

[49] Klein J J, Nigam B P. Dichroism of the Vacuum[J/OL]. Physical Review, 1964, 136(5B): 1540-1542. DOI: 10.1103/PhysRev.136.B1540.

[50] Ho W C G, Lai D. Atmospheres and spectra of strongly magnetized neutron stars - II. The effect of vacuum polarization[J/OL]. Mon. Not. Roy. Astron. Soc., 2003, 338(1): 233-252. DOI: 10.1046/j.1365-8711.2003.06047.x.

[51] Shabaltas N, Lai D. The Hidden Magnetic Field of the Young Neutron Star in Kesteven 79 [J/OL]. Astrophys. J., 2012, 748(2): 148. DOI: 10.1088/0004-637X/748/2/148.

[52] Caiazzo I, González-Caniulef D, Heyl J, et al. Probing magnetar emission mechanisms with X-ray spectropolarimetry[J/OL]. Mon. Not. Roy. Astron. Soc., 2022, 514(4): 5024-5034. DOI: 10.1093/mnras/stac1571.

[53] Beloborodov A M. Gravitational bending of light near compact objects[J/OL]. Astrophys. J. Lett., 2002, 566: L85-L88. DOI: 10.1086/339511.

[54] Ventura J. Scattering of light in a strongly magnetized plasma[J/OL]. Phys. Rev. D, 1979, 19: 1684-1695. https://link.aps.org/doi/10.1103/PhysRevD.19.1684.

[55] Meszaros P. High-energy radiation from magnetized neutron stars[M]. 1992.

[56] Heyl J S, Shaviv N J, Lloyd D. The high-energy polarization-limiting radius of neutron star magnetospheres. 1. Slowly rotating neutron stars[J/OL]. Mon. Not. Roy. Astron. Soc., 2003, 342: 134. DOI: 10.1046/j.1365-8711.2003.06521.x.

[57] Wang C, Lai D. Polarization evolution in a strongly magnetized vacuum: QED effect and polarized X-ray emission from magnetized neutron stars[J/OL]. Mon. Not. Roy. Astron. Soc., 2009, 398(2): 515-527. DOI: 10.1111/j.1365-2966.2009.14895.x.

[58] Stewart R E, Dinh Thi H, Younes G, et al. Evidence of magnetospheric vacuum birefringence in the polarized X-rays of a radio magnetar[A/OL]. 2025: arXiv:2509.19446. arXiv: 2509.19446.

[59] Stewart R, Younes G A, Harding A K, et al. X-Ray Polarization of the Magnetar 1E 1841−045[J/OL]. Astrophys. J. Lett., 2025, 985(2): L35. DOI: 10.3847/2041-8213/adbffa.

[60] Arnaud K A. XSPEC: The First Ten Years[C]//Jacoby G H, Barnes J. Astronomical Society of the Pacific Conference Series: Vol. 101 Astronomical Data Analysis Software and Systems V. 1996: 17.

[61] Arnaud K, Dorman B, Gordon C. XSPEC: An X-ray spectral fitting package[CP/OL]. 1999.

[62] Zhang S, Feroci M, Santangelo A, et al. eXTP: Enhanced X-ray Timing and Polarization

mission[C/OL]//den Herder J W A, Takahashi T, Bautz M. Society of Photo-Optical Instrumentation Engineers (SPIE) Conference Series: Vol. 9905 Space Telescopes and Instrumentation 2016: Ultraviolet to Gamma Ray. 2016: 99051Q. DOI: 10.1117/12.2232034.

[63] Zhang S, Santangelo A, Feroci M, et al. The enhanced X-ray Timing and Polarimetry mission—eXTP[J/OL]. Science China Physics, Mechanics, and Astronomy, 2019, 62(2): 29502. DOI: 10.1007/s11433-018-9309-2.

Appendix A AI Usage and Integrity Statement

毕业设计（论文）标题:

磁星 X 射线偏振谱: 超强磁场环境下辐射传输与真空量子效应研究

学生姓名：郭图 学号：522072910011 指导教师：赖东

一、本文使用的 AI 工具清单

序号[a]	AI 工具名称	版本/型号	毕业设计（论文）中应用部分[b]	人为判断过程[c] 说明
1	GPT	o3	C2	通过数学物理表达式详细给出数值代码的执行方式, 并在输出代码后进行人工复查
2	GPT	5.0-thinking	D3	撰写论文初稿之后进行学术英语润色, 输出润色结果后重新阅读并进行人工重新修改
3	GPT	5.5-thinking	E3	对论文的科学成果进行评估反馈, 模拟论文评审成果

注释:

[a] 可以根据实际情况增删行数;

[b] 可以对照“应用部分对照表”填写对应的编号表，若超过编号表内容，请根据实际填写;

[c] 人为判断过程指的是依据何种方式判断 AI 工具生成的内容的准确性。

毕业设计（论文）中应用部分对照表

A. 研究准备阶段	A1. 选题与方向设定；A2. 文献检索与筛选
B. 研究设计阶段	B1. 研究思路设计；B2. 方法论构建；B3. 研究工具开发
C. 研究实施阶段	C1. 实验/数据分析；C2. 代码编写与调试；C3. 数学建模与计算
D. 论文写作阶段	D1. 大纲与逻辑优化；D2. 论文正文写作；D3. 语言与语法润色
E. 其他辅助环节	E1. 参考文献与格式；E2. 图表/多媒体生成；E3. 学术反馈与模拟答辩

二、使用说明

（针对对应序号，简述人工智能工具如何辅助和启发研究，例如："1. A2：DeepSeek 协助综述部分框架搭建，关键观点均经文献核实；2. C2：GitHub Copilot 用于 Python 数据清洗代码的初步生成，人工调整后实现功能。"）

1. C2：GPT-o3 通过数学物理表达式详细给出数值代码的执行方式，并在输出代码后进行人工复查
2. D3：GPT-5.0 撰写论文初稿之后进行学术英语润色，输出润色结果后重新阅读并进行人工重新修改
3. E3：GPT-5.5 用于模拟论文评审过程，提供反馈意见，人工分析后对论文内容进行改进

学术诚信声明

本人承诺：论文核心观点、实验数据及结论均独立完成，AI 工具仅用于辅助性工作，已明确说明所有生成内容并在文中对应位置进行脚注标注。

承诺人： 

日期：2026 年 06 月 08 日

Research Projects and Publications during Undergraduate Period

[1] Guo T, Han C, Wang W, et al. Power corrections in the determination of heavy meson LCDAs: A renormalon-based estimation[J]. Physical Review D, 2025, 112(1): 016013.

[2] Miao T, Dai J, Liu J, et al. PhysMaster: Building an Autonomous AI Physicist for Theoretical and Computational Physics Research[J]. arXiv preprint, 2025: arXiv: 2512.19799.

[3] Guo T, Lai D. Impact of Resonant Compton Scattering on Magnetar X-Ray Polarization with QED Vacuum Resonance[J]. arXiv preprint, 2026: arXiv:2603.08119.

[4] Miao T, Jin W, Zhang M, et al. PRL-BENCH: A Comprehensive Benchmark for Evaluating the Capabilities of LLMs in Frontier Physics Research[J]. arXiv: 2604.15411. ICML 2026 accepted.

[5] Guo T, Lai D. Beyond Cassini States: Analytical Framework for Non-Trivial Obliquity Steady States in Multi-Planetary Super-Earth Systems[J]. ApJ in preparation, 2026.

[6] Guo T, Lai D. Observable Repeating Partial Tidal Disruption Events from Loss-Cone Scattering: The Role of Chaotic Tides[J]. ApJ in preparation, 2026.

Acknowledgements

本课题的研究工作是在赖东（Dong Lai）教授的悉心指导下完成的。作者在此衷心感谢赖老师对个人学习与研究能力的认可，感谢赖老师在研究思路、研究范式以及论文写作等方面给予的启发性引导与深入指导。学术前路漫漫，高山仰止；作者追随赖老师的步伐，常觉瞻之在前，忽焉在后。赖老师是一位兼具深刻物理洞见与高远学术视野的百科全书式导师，同时又极富耐心与亲和力，能够因材施教，循循善诱。赖老师博我以文，约我以礼，不愤不启，不悱不发；在给予学生充分学术自由的同时，也切实培养了学生独立开展研究的能力，并在言传身教之中涵养了学生的学术品味与国际化视野。作者衷心希望在未来与赖老师的相处和学习中，继续获得更全面的学术训练，积累更深厚的学术素养，培养更独到而深入的学术品味。相同主题的论文在投稿至 The Astrophysical Journal 的审稿过程中，获得了一位匿名审稿人的深入指导。作者在此感谢这位审稿人细致而深入的审阅，感谢他/她基于领域前沿的最新物理见地，对本文物理模型中诸多重要技术细节提出的独到建议，并在此一并致以诚挚谢意。

回顾本人整个本科阶段的成长经历，作者也尤其感谢物理与天文学院的刘世勇老师和王伟老师。两位老师虽各自肩负繁重的科研、教学与行政事务，却始终对本人的学习与科研发展给予了莫大的关怀、深入的指引与切实的支持。

刘世勇老师自引导我报名上海交通大学强基计划伊始，便在入学以来关于科研方向的讨论、前沿课程的选修、科研活动的参与，乃至日常生活状态与成长表现等方面，对作者给予了持续而深切的关心。除此之外，刘老师对教学质量高度负责的态度，以及堪称学院课程质量标杆的教学水平，也始终是作者在治学态度与工作态度上的重要榜样。

王伟老师则是作者在科研道路上的启蒙导师。自本科第二学年开始，王老师便在量子场论学习、科学前沿、领域概况以及学术生态等方面，为作者提供了深入而坦诚的指导。作者也感谢在大三学年，王老师主动引领作者接触学术前沿，并指导作者参与课题组研究，共同完成了一篇发表于 Physical Review D 的学术论文。王伟老师虽在学术界卓有成就，却始终保持着亲和、真实而平等的相处姿态。两年来的交流与相处，不仅奠定了作者的学术底色，也给予了作者面向未来的信心。

此外，作者也要感谢致远学院 2025 届毕业生俞方远学长。在作者对未来方向

一度极为迷茫之时，感谢俞学长向作者介绍天体物理领域的基本图景，并大力推荐作者加入赖老师的课题组，陪伴作者度过了学术方向过渡中的一段晦暗时期。作者同时感谢致远学院 2026 届张政亮同学。本人在本科阶段与你的相处中获得了许多陪伴、启发与引领，并得以接触常人难以企及的视角与认知。虽然我们在学术兴趣上并不完全重叠，但仍由衷感谢你以近乎同龄人的身份，给予作者非同一般的托举。感谢致远学院 2026 届苗庭嘉同学，你所从事的 AI for theoretical physics 研究方向，为作者热情地提供了诸多跨领域交叉研究的机会，使作者在人工智能迅猛发展、日新月异的岁月里，能够第一时间追近时代前沿。

感谢本科四年经历中相遇的各位朋友，感谢各个课题组的前辈与师兄师姐：王老师课题组施瑀基教授、曾军教授、张家璐博士，赖老师课题组刘彬（Bin Liu）教授、苏宇博（Yubo Su）博士、李佳儒（Jiaru Li）博士、杨孟奇、黄秀敏等；感谢各位同门潘屹涛、赵心怡等同学；感谢李政道研究所天文与天体物理研究部 Lau Jun Yan（刘俊言）等博士后朋友；也感谢访问学者武延庆（Yanqin Wu）教授和鲁文宾（Wenbin Lu）教授等。大家每一位都是组会中闪耀的学术星光，也各自在领域中具有独特的积累、见解与风采。感谢赖老师课题组诸位成员的共同努力，将课题组建设成为一个充满学术活力、开放精神与温暖氛围的大家庭。感谢萍水相逢的中科大巩钊（Anti-entropy）学长等朋友，与你们的相处既快乐亦充满启发。未来博士生涯漫长，愿能与大家继续砥砺前行，共同进步，继续追寻各自心中的理想。

感谢成长至今始终托举作者的父母，感谢给作者带来快乐与支持的姐姐。温暖的家庭始终是作者最坚实的后盾。感谢我的女朋友，一份健康而真挚的感情，会使人在内心的宁静中涌现长久的动力。感谢几位自中学时代起便长久联系的朋友常新乐、郝柏渊、蒋欣陬等，也感谢大学阶段结识的各位新朋友。道路的分歧不会将我们真正分隔，愿我们在未来长久相伴，继续见证彼此的成长。